scientific reports

Check for updates

OPEN

Early porosity generation in organic-sulfur-rich mudstones

Levi J. Knapp[1,4]✉, Omid H. Ardakani[2,3], Julito Reyes[2] & Kazuaki Ishikawa[1]

High total organic sulfur (TOS) content (i.e., Type IIS kerogen) is well known to significantly influence kerogen transformation but the effect of TOS content on the evolution of organic porosity has only rarely and indirectly been investigated. This study demonstrates that organic porosity is generated at lower thermal maturity in mudstones containing Type IIS kerogen relative to those with Type II kerogen. To our knowledge this phenomenon has not been previously demonstrated. The implications are relevant for the characterization of organic-rich mudstones as cap rocks, hydrocarbon reservoirs, and disposal reservoirs for CO_2 or nuclear waste because pore systems control storage volumes and matrix fluid flow. Five thermally immature core samples were selected from three organic-rich mudstone units with low to high TOS content: the late Devonian Duvernay Formation (Canada), middle late Miocene Onnagawa Formation (Japan), and early Jurassic Gordondale member of the Fernie Formation (Canada). Hydrous pyrolysis was used to artificially mature splits of the immature samples to four maturity stages, upon which petrophysical and organic geochemical properties were measured and compared to baseline immature samples. Most porosity growth in Type IIS samples occurred below 0.70% VRo_{eqv}, but in Type II samples was broader and robust until 1.1% VRo_{eqv}.

Organic matter (OM)-hosted porosity ("organic porosity") in self-sourced, unconventional shale oil and gas reservoirs typically dominates over inorganic porosity, and as such can critically influence hydrocarbon storage volume, adsorption capacity, permeability, and wettability[1,2]. Organic porosity becomes dominant as burial diagenesis eliminates much of the primary inorganic porosity through compaction, grain re-orientation, ductile deformation[3–5], and cementation[6–10], while secondary organic porosity is created through transformation of convertible kerogen and bitumen into liquid and gaseous hydrocarbons[11–18]. Additionally, inorganic pores can be extensively occluded when viscous bitumen and oil migrate into those pores and then undergo secondary thermal cracking into lighter fluid hydrocarbons and residual solid bitumen and pyrobitumen[14,16,19–24]. However, significant variations in organic pore volume, pore size distribution, and morphology have been documented at every observable scale.

The first order control on organic porosity is thermal maturity. Primary kerogen porosity tends to become compacted and/or occluded, but the transformation of kerogen and bitumen into liquid and gaseous hydrocarbons generates extensive secondary porosity in the residual solid OM[11–16,25,26]. The secondary control on organic porosity is effective stress. In the absence of a sufficiently rigid mineral matrix, overburden or tectonic stress will compress OM, drive out liquid hydrocarbons, and reduce OM-hosted porosity[7,25–29]. Lastly, organic porosity development is also influenced by OM type and composition, most easily observed as the absence of secondary porosity in some zooclasts such as chitinozoan and graptolite[30,31] and terrestrial OM (i.e., vitrinite and inertinite)[32]. There is a wealth of literature demonstrating that high total organic sulfur (TOS) content (i.e., Type IIS kerogen) significantly influences kerogen transformation kinetics[33–39], however the effect of TOS content on organic porosity evolution has only rarely and indirectly been investigated[40].

This study investigated the influence of TOS content on the evolution of organic porosity and pore-occluding solid bitumen by using hydrous pyrolysis (HP) to artificially mature a set of immature organic-rich mudstones with a range of TOS content, and subsequently ascertain the changes in their respective geochemical and petrophysical properties. The motivation for this research was to further delineate OM compositional controls on pore system evolution and provide insight for the evaluation of shales with Type IIS kerogen as cap rocks, unconventional hydrocarbon reservoirs, and storage reservoirs for CO_2 or nuclear waste. Five thermally immature core samples were selected from three organic-rich mudstone units, which in order of increasing TOS content were the late Devonian Duvernay Formation (Canada), middle-late Miocene Onnagawa Formation (Japan), and early Jurassic Gordondale (formerly Nordegg) member of the Fernie Formation (Canada).

[1]Japan Organization for Metals and Energy Security (JOGMEC), Chiba, Japan. [2]Natural Resources Canada, Geological Survey of Canada, Calgary, Canada. [3]Department of Geoscience, University of Calgary, Calgary, Canada. [4]Present address: Alberta Energy Regulator, Edmonton, Canada. ✉email: knapplevij@gmail.com

Results

Characterizing thermally immature samples. *X-ray diffraction.* Mineralogy of immature samples strongly varies between sample families (Table 1). DVRN1 is dominated by quartz and aluminosilicate minerals such as illite and potassium feldspar. DVRN2 is highly calcareous with subsidiary quartz. ONNA is dominated by quartz. GORD1 is calcareous-siliceous. GORD2 is a mixture of quartz, potassium feldspar, and dolomite.

Total sulfur speciation and programmed pyrolysis. Total sulfur (TS), total organic sulfur (TOS), sulfur associated with pyrite (Fe-S), and sulfur associated with kerogen (i.e., S2-OS) were measured for all samples (Table 2) using programmed pyrolysis (Rock-Eval 7S). The calculated sulfur index (SI) varies from 10.5 to 158.1 (mg TOS/TOC) which classifies Gordondale (GORD) and Onnagawa (ONNA) samples as sulfur-rich kerogen (Type IIS) and Duvernay (DVRN) samples as Type II kerogen (Fig. 1A). The ONNA immature sample has the lowest TOC

Formation	Sample family	Quartz	Plagioclase	K-feldspar	Calcite	Dolomite	Kaolinite	Illite/smectite/mica	Pyrite	Total
		wt%	wt%	wt%	wt%	wt%	wt%	wt%	wt%	wt%
Duvernay	DVRN1	32.5	–	22.3	15.7	–	3.6	22.6	3.3	100.0
Duvernay	DVRN2	18.6	–	–	57.2	9.3	3.7	10.4	0.9	100.1
Onnagawa	ONNA	88.1	–	–	–	–	–	10.3	1.6	100.0
Gordondale	GORD1	28.7	–	12.0	29.5	16.6	–	11.1	2.0	99.9
Gordondale	GORD2	34.9	4.1	27.3	–	20.9	–	11.1	1.7	100.0

Table 1. Results of X-ray diffraction (XRD) mineralogy for immature samples.

Formation	Sample family	Depth	TS	TOS	S2-OS	Residual-OS	Fe-S	Carbonates	Pyrite	Sulfur Index (SI)
		m	wt%	wt%	wt%	wt%	wt%	wt%	wt%	PyTOSx1000/TOC
Duvernay	DVRN1	2413.15–2413.30	3.82	0.78	0.19	0.58	1.91	10.00	3.80	25.61
Duvernay	DVRN2	2414.00–2414.40	1.17	0.20	0.10	0.15	0.24	57.42	0.48	10.50
Onnagawa	ONNA	16.57–16.73	2.58	0.52	0.39	0.10	1.72	0.58	3.43	127.73
Gordondale	GORD1	924.70–924.85	4.95	2.66	2.58	0.02	0.91	32.17	1.81	158.08
Gordondale	GORD2	926.00–926.15	5.42	3.42	2.96	0.41	1.53	19.00	3.05	154.99

Table 2. Sulfur content of organic and inorganic phases of studied samples measured by Rock-Eval7S programmed pyrolysis.

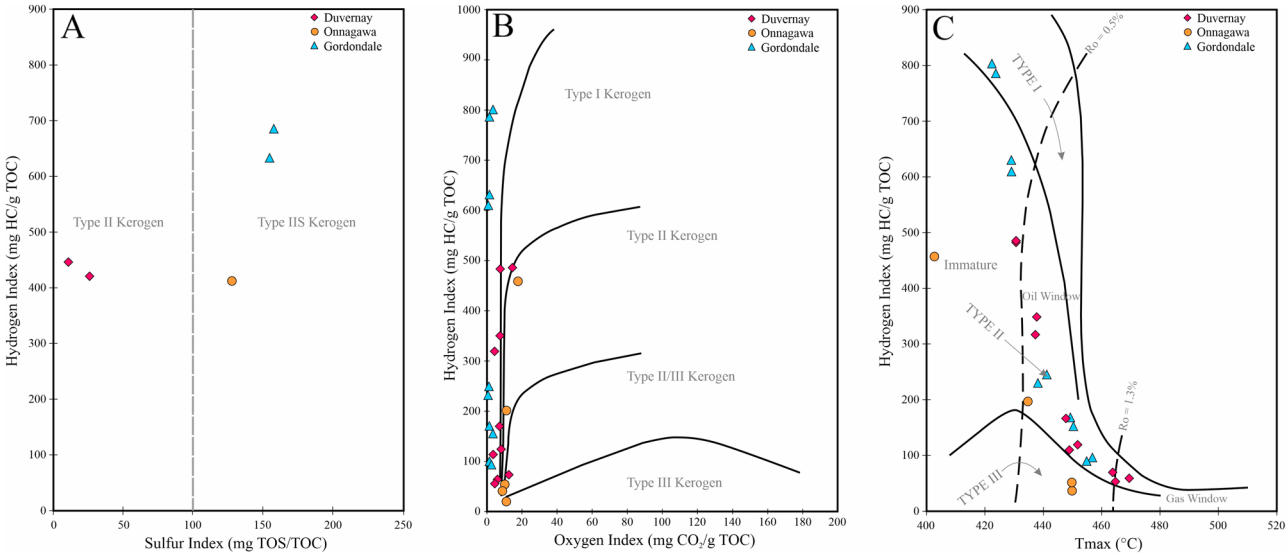

Figure 1. (**A**) Hydrogen index (HI) versus sulfur index (SI) of the studied samples based on sulfur speciation using Rock–Eval 7S. Gordondale and Onnagawa samples contain organic matter characterized as Type IIS kerogen while Duvernay organic matter is Type II kerogen. (**B**) Hydrogen index (HI) versus oxygen (OI). (**C**) HI versus Tmax plots of the studied samples. All original samples contain immature marine kerogen.

Sample family	Hydrous pyrolysis temperature and duration	S1	S2	PI	S3	Tmax	PC	TOC	RC	HI	OI	PC/TOC	VR_{eqv}	S2-loss Ø
		mg HC/g	mg HC/g	S1/(S1 + S2)	mg CO_2/g	°C	wt%	wt%	wt%	mg HC/g TOC	mg CO2/g TOC			vol%
DVRN1	Immature	3.34	36.04	0.08	0.61	431	3.37	7.46	4.09	483	8	0.45	0.65	
	310 °C × 3 days	1.41	19.15	0.07	0.31	438	1.78	6.01	4.24	319	5	0.30	0.75	4.2
	340 °C × 3 days	3.13	6.51	0.32	0.28	449	0.86	5.79	4.94	112	4	0.15	0.92	3.1
	350 °C × 3 days	0.67	3.02	0.18	0.31	465	0.35	5.45	5.11	55	5	0.06	1.17	0.9
	350 °C × 9 days	2.92	3.21	0.48	0.40	470	0.56	5.17	4.62	62	7	0.11	1.24	0.0
DVRN2	Immature	2.28	21.11	0.10	0.66	431	2.02	4.34	2.32	486	15	0.47	0.65	
	310 °C × 3 days	0.61	12.23	0.05	0.30	438	1.12	3.49	2.37	351	8	0.32	0.75	2.2
	340 °C × 3 days	1.48	5.50	0.21	0.26	448	0.62	3.26	2.63	169	8	0.19	0.91	1.7
	350 °C × 3 days	1.37	3.74	0.27	0.27	452	0.46	3.05	2.59	122	9	0.15	0.97	0.4
	350 °C × 9 days	1.01	2.17	0.32	0.40	464	0.30	2.99	2.69	73	13	0.10	1.15	0.4
ONNA	Immature	0.35	13.85	0.02	0.56	403	1.24	3.01	1.78	459	18	0.41	0.22	
	310 °C × 3 days	0.38	4.65	0.08	0.28	435	0.45	2.33	1.88	200	12	0.19	0.71	2.3
	340 °C × 3 days	0.28	1.13	0.20	0.24	450	0.15	2.08	1.94	54	11	0.07	0.94	0.9
	350 °C × 3 days	0.32	0.94	0.26	0.23	450	0.13	2.34	2.20	40	9	0.06	0.94	0.0
	350 °C × 9 days	0.22	0.45	0.33	0.27	561	0.08	2.23	2.15	20	11	0.04	2.63	0.1
GORD1	Immature	5.52	165.62	0.03	0.93	423	14.59	20.61	6.02	803	4	0.71	0.53	
	310 °C × 3 days	24.73	118.13	0.17	0.45	430	12.17	18.70	6.54	632	2	0.65	0.62	11.8
	340 °C × 3 days	65.93	42.02	0.61	0.26	439	9.20	18.08	8.88	232	1	0.51	0.76	19.0
	350 °C × 3 days	9.73	14.43	0.40	0.42	451	2.08	9.30	7.22	155	4	0.22	0.95	6.9
	350 °C × 9 days	8.41	8.46	0.50	0.33	455	1.47	9.03	7.57	93	3	0.16	1.01	1.5
GORD2	Immature	6.61	190.35	0.03	0.68	424	16.78	24.17	7.39	787	2	0.69	0.54	
	310 °C × 3 days	21.47	117.39	0.15	0.29	430	11.83	19.21	7.38	611	1	0.62	0.62	18.2
	340 °C × 3 days	23.26	32.04	0.42	0.27	442	4.72	12.94	8.21	248	2	0.36	0.81	21.3
	350 °C × 3 days	18.79	20.64	0.48	0.32	450	3.38	12.11	8.74	170	2	0.28	0.93	2.8
	350 °C × 9 days	9.82	10.61	0.48	0.28	457	1.76	10.63	8.86	99	2	0.17	1.04	2.5

Table 3. Basic programmed pyrolysis results and estimated S2-loss porosity (S2-loss Ø) of immature and artificially-matured samples. S2-loss Ø is vol% change in S2 in each sample relative to the preceding sample in the maturity series. $S2_{wt\%} = S2 \times 0.083$[41]. $S2_{vol\%} = S2_{wt\%} \times 3$ (assumes constant S2 OM density = 1/3 of matrix density).

content (3.01 wt%) among all samples. DVRN and GORD samples contain 4.34 and 7.46 wt%, 20.61 and 24.17 wt% TOC, respectively (Table 3). The hydrogen (HI) and oxygen (OI) indices of the initial immature samples vary from 459 to 803 mg HC/g TOC and 1 to 18 mg CO_2/g TOC, respectively indicating marine-sourced OM (Fig. 1B). The Tmax of the initial samples varies from 403 to 431 °C indicating all initial samples contain thermally immature marine kerogen (Fig. 1C).

Organic petrology. Onnagawa Formation. The dominant organic macerals in the Onnagawa sample (Fig. 2) are alginite with minor vitrinite. Some alginite were transformed *in-situ* to bituminite and solid bitumen while the majority of alginite show green to yellow fluorescence color, which indicates low thermal maturity. The average random solid bitumen reflectance (BRo) is 0.22 ± 0.07% (n = 21) which is equal to 0.54% equivalent vitrinite reflectance (VRo_{eqv}), calculated using Jacob's equation[42]. Both the observed fluorescence color and measured reflectance indicates the sample is immature.

Duvernay Formation. The dominant OM in the immature Duvernay samples (Fig. 3) are bituminite (as *in-situ* bituminized algae), alginite, minor inertinite and chitinozoan fragments, and pore-filling solid bitumen[28,43]. Alginite exhibits green to yellow fluorescence color, which indicates low thermal maturity (Fig. 3). The BRo of DVRN1 and DVRN2 is 0.33 ± 0.07% (n = 150) and 0.41 ± 0.08 (n = 105), respectively. The VRo_{eqv} of DVRN1 and DVRN2 is 0.60 and 0.65% (Table 3).

Gordondale member. In comparison to ONNA and DVRN samples, GORD1 and GORD2 are very organic-rich with higher maceral type variation. The dominant macerals are alginite, bituminite, vitrinite, inertinite, solid bitumen, and exsudatinite (Fig. 4). Exsudatinite and solid bitumen mainly fill the pore space within inertinite, intergranular pores, and microfossils (Fig. 4A–F). Abundant exsudatinite and matrix bitumen (i.e., pre-oil bitumen) with dark yellow brown fluorescence were observed in both samples (Fig. 4). Alginite also show bright yellow fluorescence which indicates low thermal maturity (Fig. 4). In some cases, exsudatinite turned into solid bitumen with a polishable surface that could be distinguished under white incident light (Fig. 4E,F). There is also abundant solid bitumen, formed *in-situ* by the thermal degradation and transformation of alginite macer-

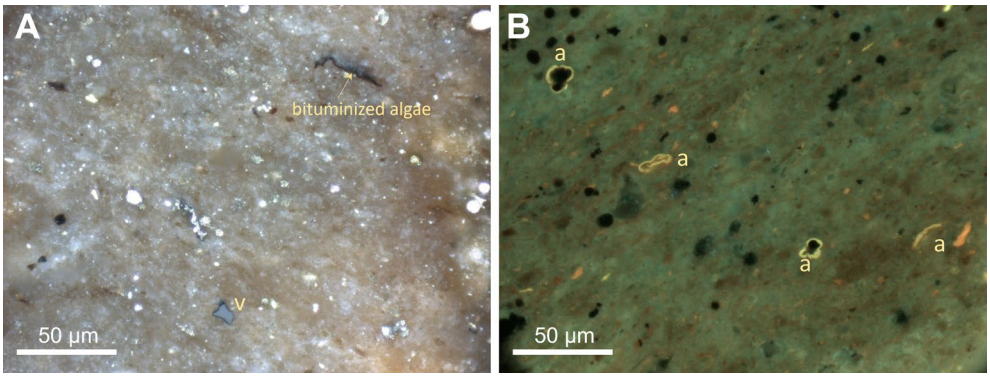

Figure 2. Photomicrographs of Onnagawa immature samples with incident white (left) and ultraviolet (UV) light (right) under oil immersion with × 50 objective. (**A**) a finely crystalline rock matrix with sporadic fine pyrite crystals, partially spent algae and vitrinite (v) particles, and (**B**) sporadic green to yellow fluorescing alginite (a) macerals.

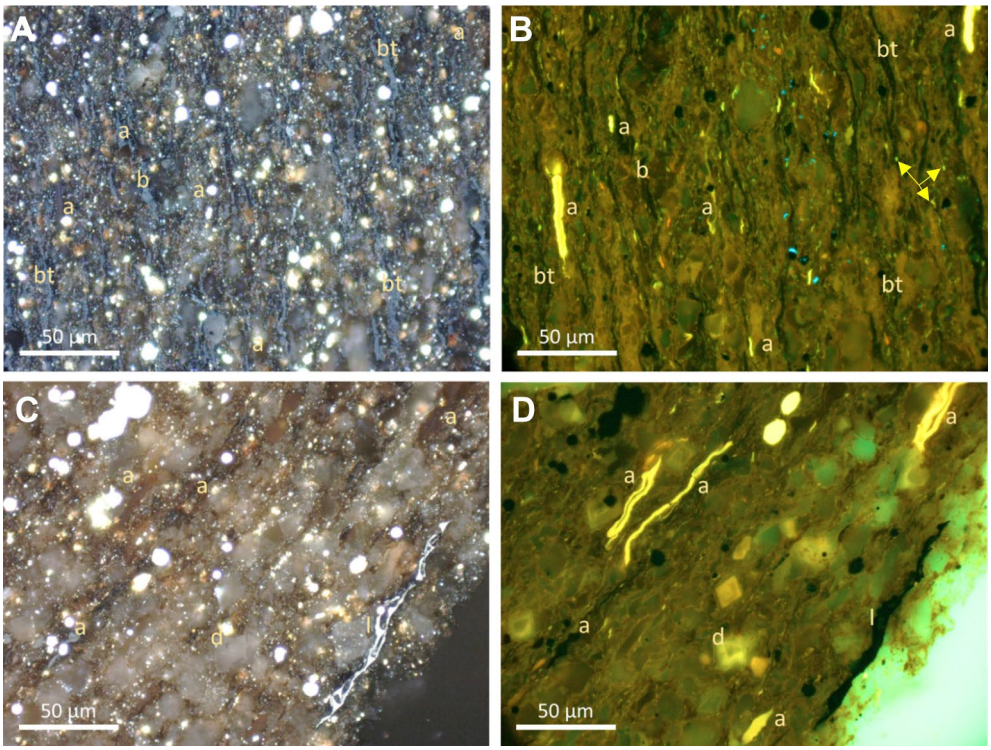

Figure 3. Photomicrographs of Duvernay immature samples with incident white (left) and ultraviolet (UV) light (right) under oil immersion with × 50 objective. (**A**, **B**) Pair view shows a fine-grained clay-rich matrix with long thin lenses of weak reddish-orange fluorescing bituminite (bt) and traces of solid bitumen (b), thin long and short lenses of greenish yellow to reddish orange fluorescing alginite (a) and liptodetrinite (arrow). (**C**, **D**) Pair view shows coarser matrix with less clay, minor amount of thin long and short lenses of greenish yellow to reddish orange fluorescing alginite (a), and traces of inertinite. Dolomite crystals (d) were also observed.

als (Fig. 4G,H). The BRo of GORD1 and GORD2 samples is 0.14 ± 0.04% (n = 145) and 0.27 ± 0.08% (n = 81), respectively, which has VRo_{eqv} of 0.49 and 0.57% (Table 3).

Geochemical changes during maturation. *Programmed pyrolysis and organic petrology.* Hydrous pyrolysis stages were conducted at isothermal temperature of 310, 340, 350 (for 3 days) and 350 °C (for 9 days) and are referred to in the text as 310 × 3, 340 × 3, 350 × 3, and 350 × 9. The variations of programmed pyrolysis parameters over the HP series of all samples are shown in Fig. S1 online. Except for S1 (free hydrocarbon) that is subject to evaporative loss (e.g.,[45]) during sample handling and preparation, the other parameters show a clear trend with increasing thermal maturity during artificial maturation (Table 2). The S2 (kerogen content) and HI show

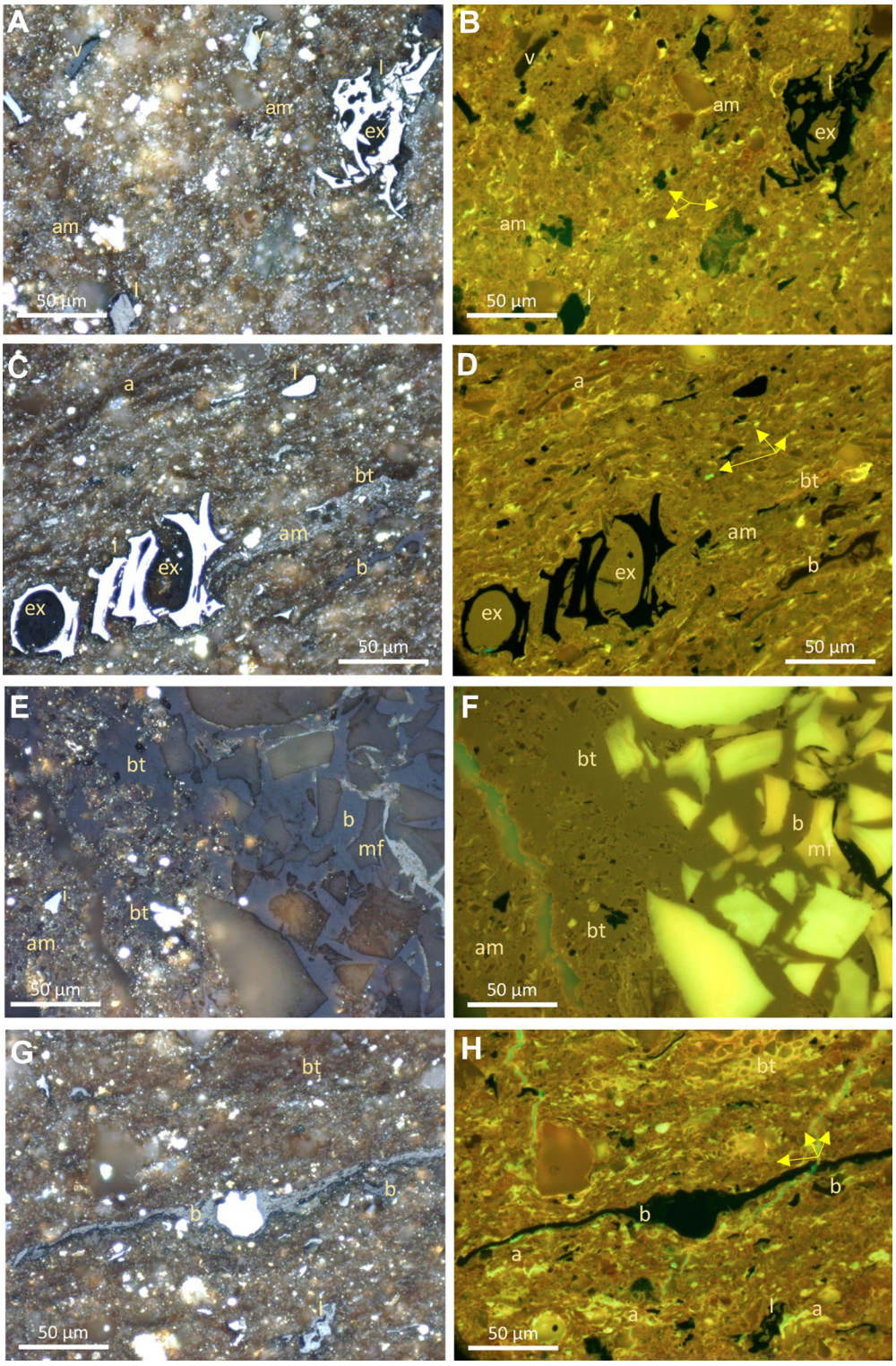

Figure 4. Photomicrographs of Gordondale immature samples observed under incident white (left) and ultraviolet (UV) light (right) under oil immersion with × 50 objective. (**A**, **B**) Pair view of abundant brown amorphous kerogen (am) and greenish-yellow to yellow fluorescing elongated thin lenses of alginite (a) and liptodetrinite (arrows), and traces of vitrinite (v), inertinite (I) and dark orange fluorescing exsudatinite (ex). (**C**, **D**) Pair view shows a laminated matrix with large orange to reddish-brown fluorescing alginite (a) and solid bitumen (b), thin lenses of greenish-yellow to yellow fluorescing alginite (a) and liptodetrinite (arrow), and weak fluorescing exudatinite (ex). (**E**, **F**) Pair view shows reddish-orange fluorescing matrix consisting of amorphous kerogen (am) bituminite (bt) and solid bitumen (b) brecciated between bright fluorescing calcareous microfossil (mf) fragments. (**G**, **H**) Pair view shows matrix with large long lenses of brown-fluorescing and small reddish-brown-fluorescing solid bitumen (b), yellow fluorescing bituminite (bt), long thin lenses of greenish-yellow to yellow fluorescing alginite (a) and liptodetrinite (arrow), traces of inertinite (I).

a consistent and sharp decline with thermal maturity advancement, while Tmax values increased consistently with increasing temperature. The ONNA sample at 350 × 9 shows anomalously high Tmax (561 °C) which is due to a low S2 yield (0.45 mg HC/g) (e.g.,[46,47]). This high value caused a significant increase in the Tmax-derived Ro value (2.63%) (Table 2). The TOC content of all samples except ONNA shows a consistent decreasing trend with thermal maturity advancement, which is consistent with thermal degradation and conversion of convertible OM into various hydrocarbon fractions.

Onnagawa Formation. The physicochemical transformation of kerogen in ONNA samples started from 310 × 3. At this stage, some of the easily convertible OM such as bituminite and alginite started to thermally transform *in-situ* to various hydrocarbon fractions (oil, viscous and solid bitumen and gas). Alginite (*Tasmanites*) with greenish fluorescence color started to change from green to dark yellow and produce small quantites of greenish-yellow fluorescing oil oozing onto the surface from the thermally degraded alginite (observed under UV light). The VRo_{eqv} increased slightly at this stage, from 0.54 to 0.68%, which is in accordance with an increase in Tmax from 403 to 435 °C (Table 4). At 340 × 3, most of the alginite transformed *in-situ* to oil, viscous and solid bitumen and its UV fluorescence color turned to dark red or in some cases totally diminished. VRo_{eqv} further increased to 1.10% with increase in Tmax from 435 to 447 °C (Table 4, Fig. S1). At 350 × 3 almost all alginite were thermally converted to solid bitumen. VRo_{eqv} increased slightly to 1.19% while the Tmax did not change. At the final stage of HP analysis (350 × 9), VRo_{eqv} further increased to 1.45%, with unreliable Tmax-derived VRo_{eqv} due to low S2 yield (Table 3).

Duvernay Formation. The physicochemical transformation of kerogen in DVRN1 and DVRN2 samples started from 310 × 3. At this stage, greenish-yellow fluorescing alginite in the immature samples started to transform *in-situ* into various hydrocarbon fractions resulting from the thermal degradation and conversion of OM. The VRo_{eqv} of DVRN1 and DVRN2 increased from 0.60 and 0.65 to 0.74 and 0.69%, respectively. The Tmax value and

Sample family	HP temperature and duration	Organic matter type							#Measured Tmax	VR_{eqv} from Tmax
		Vitrinite			Bitumen			VR_{eqv}		
		%Ro	SD	N	%Ro	SD	N	%Ro	°C	%Ro[1]
DVRN1	Immature	na	na	na	0.33	0.07	150	**0.60**	431	0.60
	310 °C × 3 days	0.77	0.07	23	0.54	0.08	18	**0.74**	438	0.72
	340 °C × 3 days	1.08	0.10	11	1.06	0.20	40	**1.06**	450	0.94
	350 °C × 3 days	na	na	na	1.41	0.17	50	**1.27**	463	1.17
	350 °C × 9 days	na	na	na	1.54	0.17	51	**1.35**	471	1.32
DVRN2	Immature	na	na	na	0.41	0.08	105	**0.65**	431	0.60
	310 °C × 3 days	0.72	0.08	45	0.46	0.10	24	**0.69**	438	0.72
	340 °C × 3 days	1.08	0.06	12	1.13	0.15	44	**1.10**	450	0.94
	350 °C × 3 days	1.18	0.07	5	1.40	0.14	49	**1.27**	454	1.01
	350 °C × 9 days	na	na	na	1.65	0.18	76	**1.42**	504	1.91
ONNA	Immature	na	na	na	0.22	0.06	21	**0.54**	403	0.09
	310 °C × 3 days	0.71	0.05	14	0.45	0.09	16	**0.68**	435	0.67
	340 °C × 3 days	1.20	0.02	2	1.14	0.11	29	**1.10**	447	0.88
	350 °C × 3 days	na	na	na	1.28	0.18	37	**1.19**	446	0.87
	350 °C × 9 days	na	na	na	1.64	0.15	48	**1.41**	562	2.96
GORD1	Immature	na	na	na	0.14	0.04	145	**0.49**	423	0.45
	310 °C × 3 days	na	na	na	0.72	0.09	33	**0.70**	430	0.58
	340 °C × 3 days	0.90	0.08	13	0.82	0.05	13	**0.90**	446	0.87
	340 °C × 3 days	*na*	*na*	*na*	*0.52*	*0.12*	*40*	*0.72*	*446*	*0.87*
	350 °C × 3 days	0.97	0.07	12	1.11	0.13	36	**1.08**	454	1.01
	350 °C × 9 days	1.25	0.02	2	1.56	0.18	56	**1.37**	464	1.19
	350 °C × 9 days	*na*	*na*	*na*	*1.73*	*0.44*	*36**	*1.47*	*464*	*1.19*
GORD2	Immature	na	na	na	0.27	0.08	81	**0.57**	424	0.47
	310 °C × 3 days	0.72	0.06	18	0.42	0.10	8	**0.66**	433	0.63
	340 °C × 3 days	0.90	0.12	11	0.98	0.12	31	**1.01**	443	0.81
	350 °C × 3 days	1.13	0.06	10	1.10	0.11	38	**1.08**	453	0.99
	350 °C × 9 days	1.25	0.08	3	1.53	0.14	69	**1.35**	470	1.30

Table 4. Measured vitrinite reflectance, bitumen reflectance and %VR equivalent, and %VRo from Tmax. Bolded $\%VRo_{eqv}$ values were used for plotting against porosity data. Italicized data indicate secondary populations of bitumen. na: no measured vitrinite particles, #average of two to three measurements, *anisotropic fine-grained mosaic pyrobitumen, [1]VR_{eqv} based on Tmax[44].

Tmax-derived VRo_{eqv} also showed the same increasing trend (Table 4, Fig. S1). At 340 × 3 the fluorescence color of alginite continued to shift from yellow to dark yellow to orange with further thermal cracking. Generated solid bitumen started to fill pores within the matrix and OM. The first evidence of generated oil was observed under UV light. The amount of solid bitumen and produced oil observed in DVRN samples is significantly higher than ONNA samples. The VRo_{eqv} of DVRN1 and DVRN2 increased to 1.06 and 1.10%, respectively. At 350 × 3, almost all alginite and amorphous OM were completely transformed to various hydrocarbon fractions dominated by oil and solid bitumen. The VRo_{eqv} increased to 1.27 and 1.19% for DVRN1 and DVRN2, respectively (Table 3, Fig. S1). At 350 × 9, the fluorescence color of alginite completely diminished and the adsorbed oil exuded onto the sample surface when exposed to UV light. Solid bitumen was the most observed maceral at 350 × 9. VRo_{eqv} increased to 1.35 (DVRN1) and 1.42% (DVRN2).

Gordondale member. The physicochemical transformation of kerogen in GORD1 and GORD2 samples started from 310 × 3 (Tmax = 430–433 °C). Alginite and matrix bitumen transformed to lighter hydrocarbons and the fluorescence intensity of residual alginite and produced solid bitumen were masked by excessive amounts of greenish-yellow fluorescing oil oozing onto the surface of the samples under UV light. GORD samples were significantly richer in inertinite compared to other samples. The VRo_{eqv} of GORD1 and GORD2 increased from 0.49 and 0.57 to 0.70 and 0.66%, respectively. At 340 × 3 the fluorescence color of alginite and matrix bitumen shifted from bright yellow to slightly darker yellow while most of the matrix bitumen and exudatinite transformed to solid bitumen. The VRo_{eqv} of both GORD1 and GORD2 increased to 0.90 and 1.01%, respectively (Table 3). A second BRo population was observed with a lower value (GORD1: 0.52 ± 0.12; n = 40) than the main population (0.82 and 0.98% BRo in GORD1 and GORD2), consistent with scanning electron microscopy (SEM) observations that show two phases of solid bitumen (described below). At 350 × 3 the VRo_{eqv} of both GORD1 and GORD2 increased to 1.08% (Table 3). At 350 × 9, more solid bitumen formed with the advancement in OM thermal cracking. The VRo_{eqv} of GORD1 and GORD2 increased to 1.37 and 1.35%, respectively (Table 4).

Textural changes during maturation. *SEM observations.* Onnagawa Formation. ONNA samples do not display significant bedding textures at SEM-scale (~ 100's µm) but typically have isolated OM particles and pyrite framboids dispersed in a porous microcrystalline quartz matrix (Fig. 5A). Pyrite framboids are often hosted within OM, with common signs of plucking. Intercrystalline pores in the microcrystalline quartz matrix are typically 10's of nm in diameter and are variably filled with OM (Fig. 6). Observable OM porosity in the immature sample (Fig. 6A) is limited to minor primary porosity, as well as shrinkage cracks at mineral–OM interfaces. Bubble-type pores, typically less than 1 µm in diameter, often occurring at mineral-OM interfaces, and sometimes exhibiting raised rims, become common at 310 × 3 and extensive by 340 × 3 (Fig. 6B,C). Bubble pores seem to be less extensive at 350 × 3, however large OM particles are limited (Fig. 6D). Bubble-type pores are common at 350 × 9 (Fig. 6E). From 340 × 3 onwards OM pore diameters are mostly limited by adjacent mineral boundaries and many OM particles exist only as residual grain-coating layers.

Duvernay Formation. Organic matter in DVRN samples occurs as large, elongate particles (DVRN1: 10's-100's µm long by < 20 µm thick; DVRN2: < 100 µm long by < 10 µm thick) and as intimate mixtures with matrix minerals (Fig. 5B,C). Observable matrix porosity is minor in immature DVRN samples and is restricted to nm-scale pores in tight clusters of clay minerals. Artificially-matured samples contain inorganic porosity within masses of fibrous Mg-rich (as confirmed by SEM–EDS; Fig. S2) diagenetic minerals, altered from dolomite. Intergranular pores between the fibers of these masses are typically 10's of nm in diameter but likely range from a few nm to a few hundred nm.

Observable OM porosity is nearly absent in the immature DVRN samples, except for shrinkage cracks and very rare bubble pores (Fig. 7A,B). The first widespread appearance of organic porosity is at 310 × 3, and intimate association of OM and authigenic minerals starts at this stage (Fig. 7C). Authigenic minerals often extend into (or are enveloped by) bubble-shaped pores, which may be anchored on mineral surfaces, sometimes have raised rims, and typically have diameters < 3 µm. Bubble pores increase in abundance to 340 × 3 (Fig. 7F), beyond which their occurrence decreases moderately (Fig. 7G–K). Two phases of bitumen, based on greyscale (average atomic mass but interpreted as density; see Methods) contrast, were observed throughout the maturity series. In immature samples irregular to wispy density variations are present within some OM particles (Fig. 7A). From 310 × 3 onwards, apparent filling of formerly open bubble pores by lower density (darker grey) bitumen occurs, increasing from minor at 310 × 3 (Fig. 7D) to common at 350 × 3 (Fig. 7H) and decreasing at 350 × 9 (Fig. 7K). The lower density bitumen phase sometimes has clusters of dimples or small pores, giving it a spongy texture, and usually does not contain floating clay particles which are common in the lighter grey host bitumen.

Gordondale member. Organic matter represents a significant proportion of the visible sample area in GORD SEM images (Fig. 5D,E). Most of the OM is bitumen, which engulfs both minerals (detrital and authigenic) and discrete OM particles (higher density, distinct edges). Observable matrix porosity is minor in immature GORD samples and is restricted to nm-scale pores in tight clusters of clay minerals. Inorganic porosity appears to increase through the maturity series, as dolomite crystals are progressively altered from rim to core into masses of fibrous Mg-rich diagenetic minerals (Fig. 8). Intergranular pores between the fibers of these masses are typically 10's of nm in diameter but likely range from a few nm to a few hundred nm. Mg-rich masses are more common in GORD than DVRN samples.

Organic porosity is minor in the immature samples (Fig. 9A,B), typically as shrinkage cracks or rare primary organic porosity. Secondary organic porosity increases to the 340 × 3 stage (Fig. 9C–F) and then decreases (Fig. 9G–K). Two main secondary OM pore types were observed: (1) large (~ 1–2 µm) bubble- or irregular-shaped

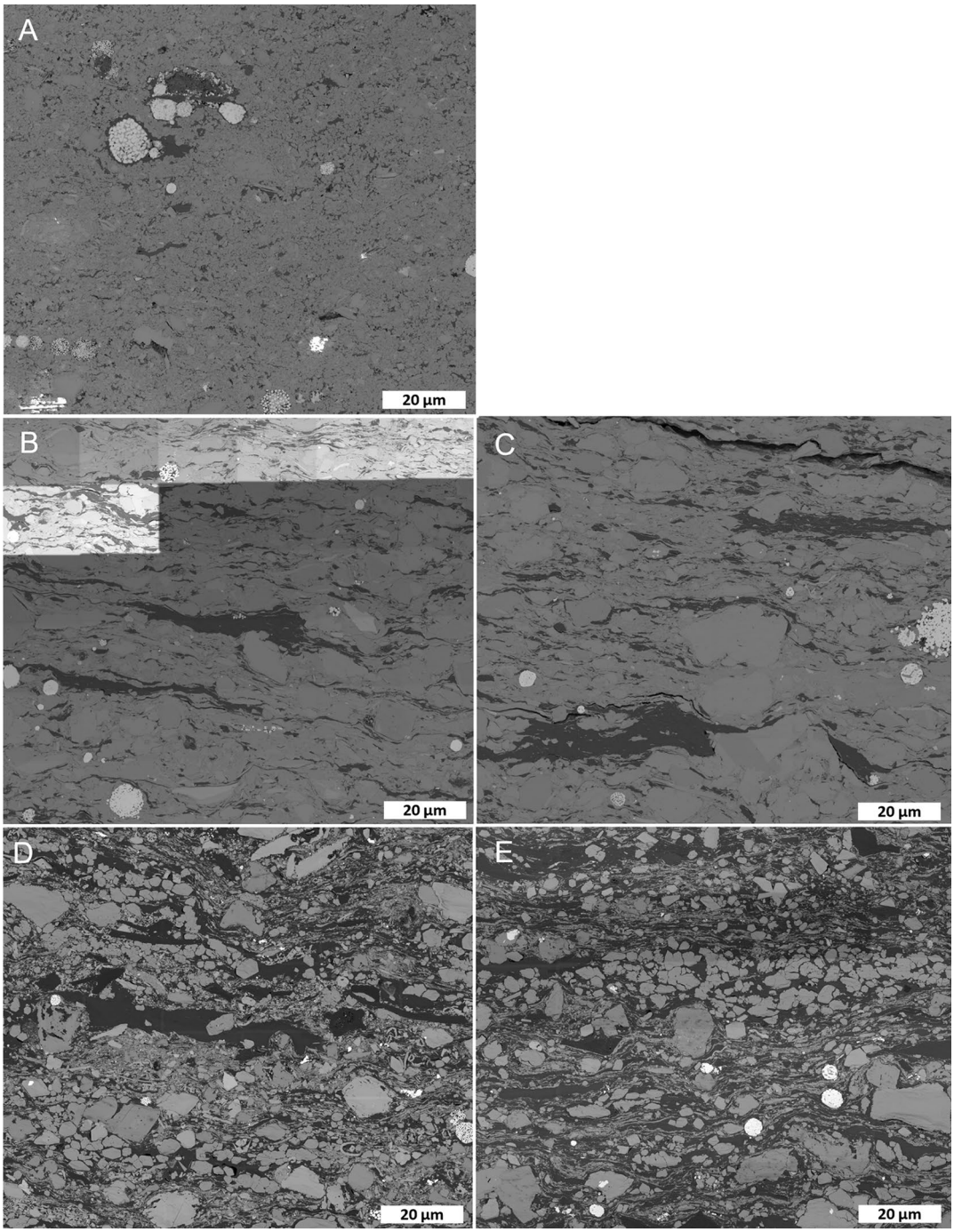

Figure 5. Backscattered electron SEM images of thermally immature samples from all sample families at overview resolution (115 nm/px). Organic matter is dark grey in the images. (**A**) ONNA. (**B**) DVRN1. (**C**) DVRN2. (**D**) GORD1. (**E**) GORD2.

pores, and (2) sponge-like clusters of ~ 100–200 nm pores, often within large regions of solid bitumen. Irregular pores are often surrounded by thick (10's-100's nm) coats of bitumen on adjacent mineral particles (Fig. 9C,J). The pore size of each pore type group appears relatively constant throughout the maturity series. At all maturity stages, and particularly from 340 × 3 onwards, two phases of bitumen are visible based on greyscale contrast. The lower density (darker) phase contains organic porosity and fluid-like textures.

MICP and N_2-adsorption. The present study analyzes the matrix pore system and thus does not utilize MICP data corresponding to > 4 µm pore throat diameter to avoid intruded volume associated with conformance, artificial fractures, and experimental artefacts. MICP (Fig. 10) and N_2-adsorption (Fig. 11) data (Table 5) show that pore volume is close to zero in immature GORD and DVRN samples, but much higher in ONNA, consistent with SEM observations that show common matrix porosity in the immature ONNA sample. Total pore volumes

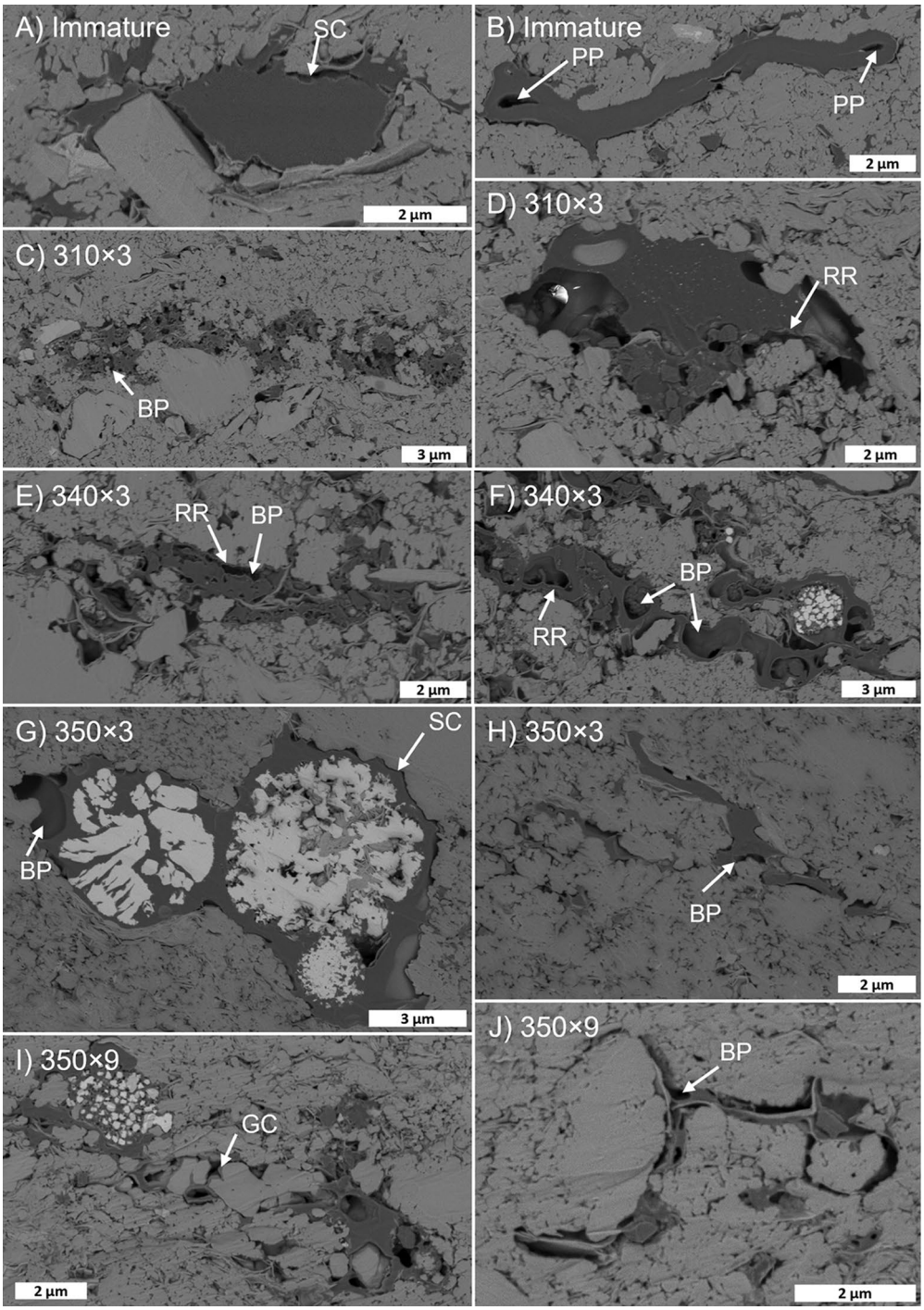

Figure 6. Onnagawa maturity series in high resolution (5 nm/px) backscattered electron SEM images. SC: shrinkage crack; PP: primary pore; BP: bubble pore; RR: raised rim; GC: grain coat.

increase significantly in all samples in response to thermal maturation. ONNA samples have the smallest growth in pore volume, followed by DVRN, then GORD, a trend consistent with increasing TOC content. Incremental porosity changes at each successive maturity stage, as estimated from MICP are consistent with those estimated from the loss of S2 (which represents the porosity-hosting OM phases) (Fig. 12). The 4 outliers are GORD1 and GORD2 samples at 340 × 3 and 350 × 3, which show extensive low-density, pore-filling solid bitumen in SEM images. The presence of extensive low-density bitumen breaks the assumption that S2 OM density is equal to 1/3 matrix density, thus overestimating S2-loss porosity. MICP pore throat size distributions (PTSD) vary significantly between sample groups (Fig. 10). Most pore volume growth for DVRN and ONNA samples occurs in pores with pore throat diameters below about 0.3 µm, with maximum amplitudes in the range of approximately 0.03 to 0.1 µm. Minor pore volume growth occurs in the pore throat range of 0.3 to 4.0 µm. Most pore volume

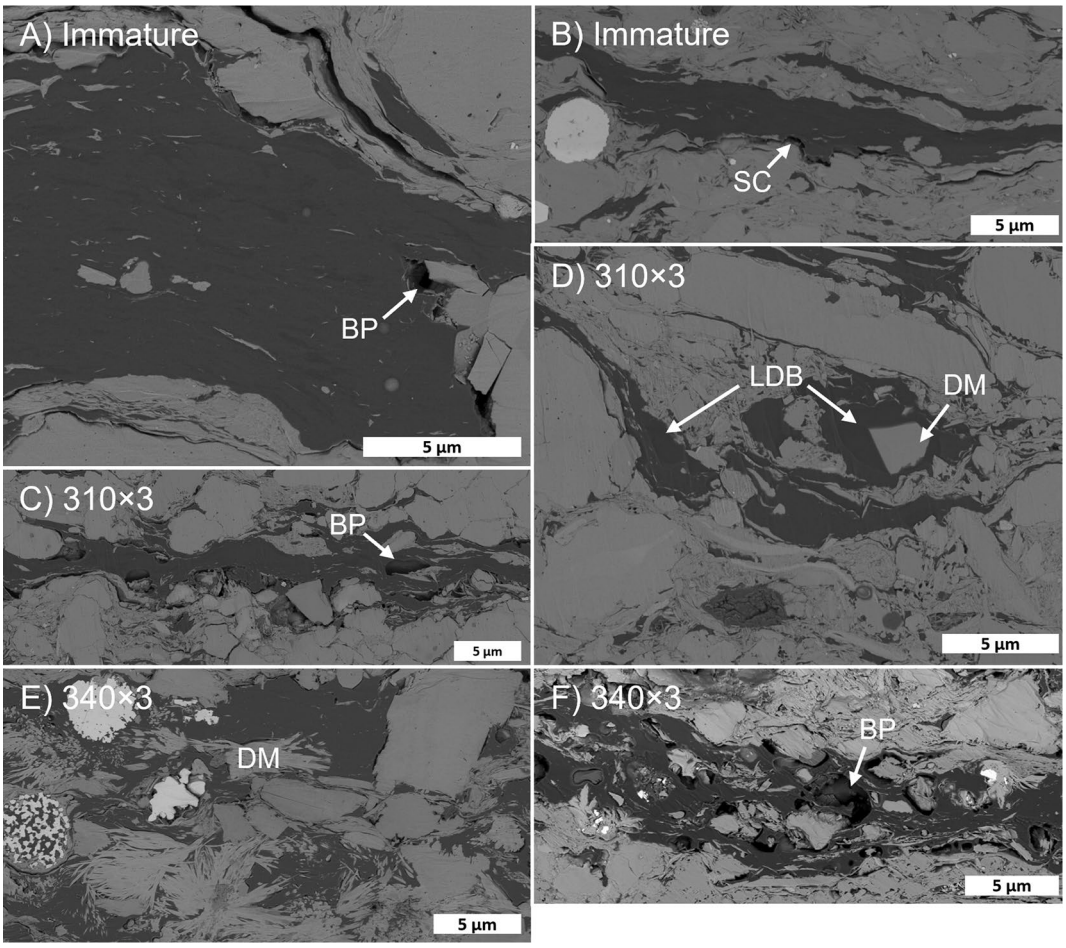

Figure 7. Duvernay maturity series in high resolution (5 nm/px) backscattered electron SEM images. SC: shrinkage crack; BP: bubble pore; RR: raised rim; GC: LDB: low density bitumen; Di: dimples; DM: diagenetic mineral.

growth for GORD samples occurs in pores with larger pore throats, below about 3.0 µm, with maximum amplitudes in the range of approximately 0.4 to 2.0 µm. DVRN and ONNA samples generally have MICP pore throat sizes much smaller than SEM-observed pore body diameters while GORD samples have MICP pore throat diameters similar to SEM-observed pore body diameters.

Pore size distributions (PSD) from N_2-adsorption (Fig. 11) are more similar across the sample groups compared to MICP PTSD. For all samples, most of the N_2 pore volume occurs in the size range of about 5–100 nm, which is the upper pore diameter limit of N_2-adsorption measurements, thus preventing detection of µm-scale bubble- and irregular-type pores. Differences in PSD are most notable in the size range of about 20–100 nm, roughly coincident with the SEM-observed pore size ranges of spongy porosity and fibrous mineral masses. In this range ONNA pore volumes generally decrease with increasing pore size and there is no significant change in volume through the maturity series (Fig. 11E). DVRN pore volumes moderately increase with increasing pore size and there is significant pore volume increase from low to high thermal maturity (Fig. 11C,D). GORD pore volumes steeply increase with increasing pore size and there is very significant pore volume increase from low- to high-thermal maturity (Fig. 11A,B). These observations are consistent with SEM observations that the occurrences of spongy porosity and porous fibrous mineral masses increase with increasing thermal maturity and are non-existent, minor/moderate, and abundant in ONNA, DVRN, and GORD, respectively. Peak pore throat diameter (PPTD), the maximum amplitude of the PTSD increases significantly in all five sample groups from immature to 310 × 3 (Fig. 10), after which PPTD increases only slightly and discontinuously towards maximum thermal maturity. PPTD decreases from 340 × 3 to 350 × 3 in DVRN and GORD samples.

The timing of pore volume growth is variable across sample sets. In Type IIS samples (GORD and ONNA), approximately 90% of the total change in MICP-detected pore volume occurs from immature to 310 × 3, and subsequent porosity change is very minor (Fig. 13A,C). Similarly, 65–85% of the total N_2 pore volume generation (Fig. 13B,D), occurs by 310 × 3 in GORD and ONNA samples. In contrast, only about 45–55% of the total MICP (Fig. 13C) and N_2 (Fig. 13D) pore volume change had occurred by 310 × 3 for the low-TOS DVRN samples, while another 30–40% occurred between 310 × 3 and 340 × 3. In terms of VRo_{eqv}, GORD and ONNA samples exhibit

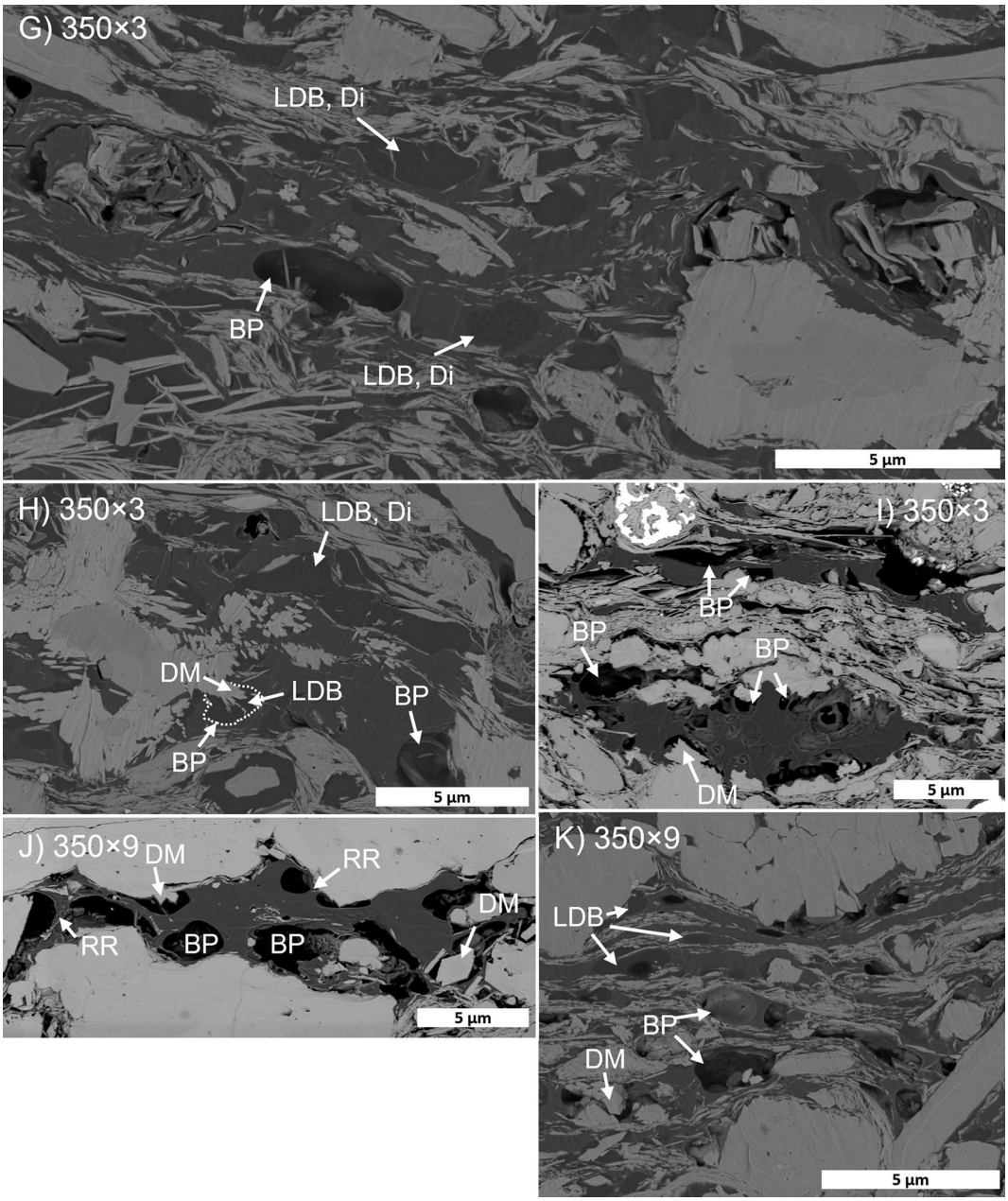

Figure 7. (continued)

the most drastic pore volume generation below about 0.70% while DVRN samples have more evenly distributed pore volume generation up to approximately 1.1% VRo_{eqv}.

Discussion

Porosity origins. Organic pores were generated in all samples during HP thermal maturation. Organic pores were observed directly in SEM images and significant pore volume increases were detected by MICP and N_2-adsorption measurements (Figs. 11, 12). The magnitude of pore volume change from immature to the final HP stage was lowest in ONNA, followed by DVRN, then GORD sample sets, consistent with increasing TOC content, suggesting pore volume growth is primarily associated with organic pores. Furthermore, incremental porosity change estimated by S2 loss is similar to estimations from MICP, indicating that pore volume change is dominated by S2 OM (Fig. 12). These observations are consistent with a large body of published research showing that thermal maturity is a first order control on organic porosity generation[11–16,48,49]. However, this study also demonstrates the generation of *inorganic* pores with increasing thermal maturity—specifically dolomite alteration to Mg-rich fibrous masses. Positive correlation between pore volume and thermal maturity in organic-rich rocks cannot always be completely attributed to organic porosity (e.g.,[50–52]). More research is warranted to understand the occurrence of similar dolomite alteration in natural settings.

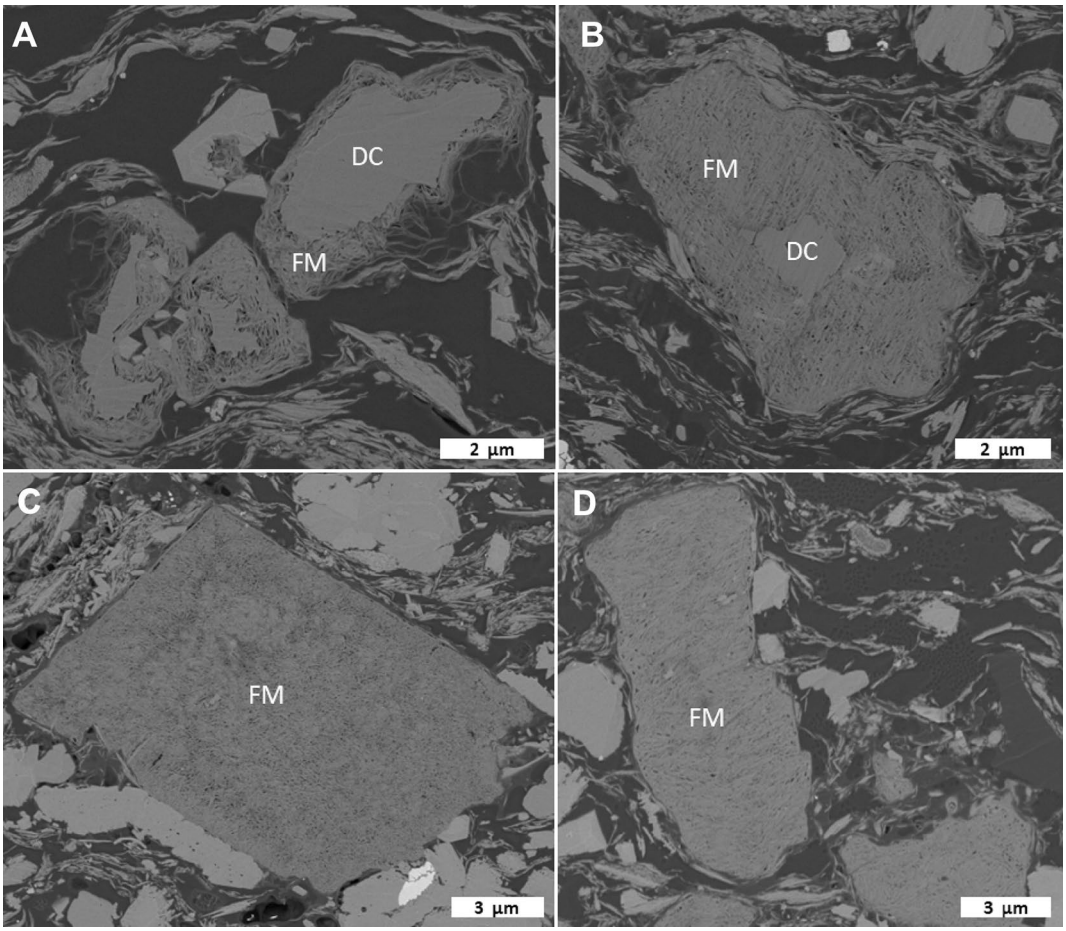

Figure 8. Progressive alteration of dolomite to Mg-rich fibrous masses in the GORD2 maturity series. Backscattered electron SEM images. (**A**) 310 × 3. (**B**) 340 × 3. (**C**) 350 × 3. (**D**) 350 × 9. DC: dolomite core; FM: fibrous mass.

Porosity destruction. There are many processes that can reduce pore volume, but these processes can be generalized as either compaction or occlusion. Compaction is not relevant to our samples as they were artificially matured without overburden load, but occlusion may be significant, particularly by oil and bitumen (i.e., migrabitumen *sensu*[42]), which can then be transformed into solid bitumen or pyrobitumen[14,16,19–21,23,53] across a wide thermal maturity range[54–56] (among others). The presence of pore-filling solid bitumen has been documented across our HP data set over a maturity range consistent with that observed in other natural[14,16,19–21,23,53] and artificial settings[57–59] Pore-filling textures are apparent in SEM (Figs. 7, 9) and organic petrographic images (Fig. 5) of all GORD and DVRN samples (0.49–1.42% VRo_{eqv}). Furthermore, at least two phases of pore-filling solid bitumen were observed in GORD samples, based on greyscale contrast in SEM images, bimodal bitumen reflectance populations, and an interpretation that outliers in a cross plot of MICP vs S2-loss porosity (Fig. 12) correspond to the generation of a voluminous low-density, pore-filling solid bitumen phase. The lower density phase of solid bitumen can sometimes be observed at low maturity but becomes much more prevalent from 340 × 3 onwards (greater than about 0.9% VRo_{eqv}) and seems to fill previously generated organic pores (e.g., Fig. 7G,H,K). These observations support the notion that the composition of pore-filling fluids (that later transform to solid bitumen) evolve with thermal maturity, as observed in laboratory[55–59] and natural settings[20,57,58]. In this case, the later solid bitumen phase is less dense. The observations additionally demonstrate that pore-occlusion by solid bitumen is not restricted to inorganic pores.

Timing of organic porosity generation and destruction. The central hypothesis of this study was that organic porosity should be generated sooner (at lower thermal maturity) in samples with high TOS content (i.e., Type IIS kerogen) as source rocks with Type IIS kerogen are known to generate oil earlier than those with low TOS content (e.g., Type II kerogen)[33–39]. The data from this study positively support the hypothesis, and we believe this work is the first published demonstration of this phenomenon. Figure 12 illustrates that in Type IIS samples (GORD and ONNA), the large majority of total pore volume increase occurs below about 0.70% VRo_{eqv}. In contrast, pore volume increase in the low-TOS DVRN samples is more broadly distributed, and robust pore volume growth continues until approximately 1.1% VRo_{eqv}, with subsequent minor increase to about 1.4% VRo_{eqv} above which we do not have data. Prolonged pore volume growth is common in artificially

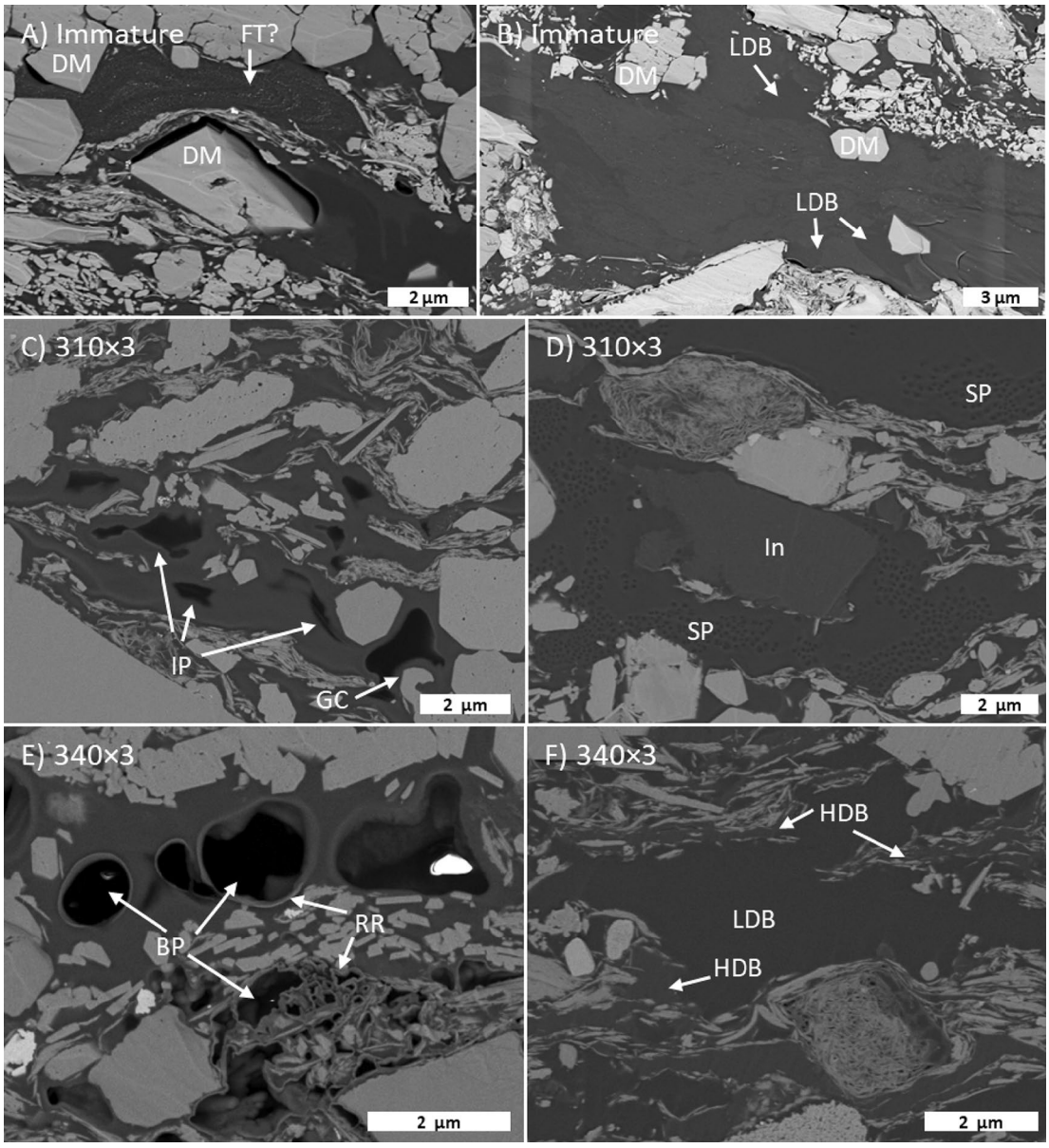

Figure 9. Gordondale maturity series in high-resolution (5 nm/px) backscattered electron SEM images. BP: bubble pore; IR: irregular pore; SP: spongy porosity; RR: raised rim; LDB: low-density bitumen; HDB: high-density bitumen; GC: grain coat; FT: flow textur;, In: inertinite; DM: diagenetic mineral.

matured organic-rich shales with low TOS concentrations[60–64]. The contrasting pore-volume trends between Type II and Type IIS samples presented here suggest that organic porosity generation occurs earlier in samples with high TOS relative to those with low TOS. These observations are evident despite the significant variation in TOC content, mineralogy, and texture between sample sets. GORD samples have drastically higher TOC values than ONNA samples, and ONNA samples have a tight microcrystalline quartz matrix drastically different from the matrix and mineralogy of GORD samples, but both sample sets exhibit a strong dominance of pore volume increase at low thermal maturity relative to the DVRN sample sets. TOS content influences porosity generation timing but not magnitude of change, which is controlled by TOC.

Organic porosity generation reported here, between ~ 0.5–1.4%VR_{eqv} is consistent with myriad studies showing secondary organic pore generation in natural systems in this maturity range[28,29] (among others), tempered by compaction, which is absent here, and occlusion by solid bitumen. Organic porosity generation is also known to occur at higher thermal maturity but was not tested in this study given the maximum maturity of ~ 1.4% VR_{eqv}. No study known to the authors has examined organic pore system evolution as a function of TOS content in natural systems. The present experimental study lays the groundwork for such research.

TOS content influences the timing of hydrocarbon and porosity generation and thus may also influence the timing of porosity destruction via pore-filling solid bitumen. Figure 12A and C show that the first occurrence of negative MICP pore volume change occurs at lower thermal maturity in Type IIS samples (1.08 and 1.10%

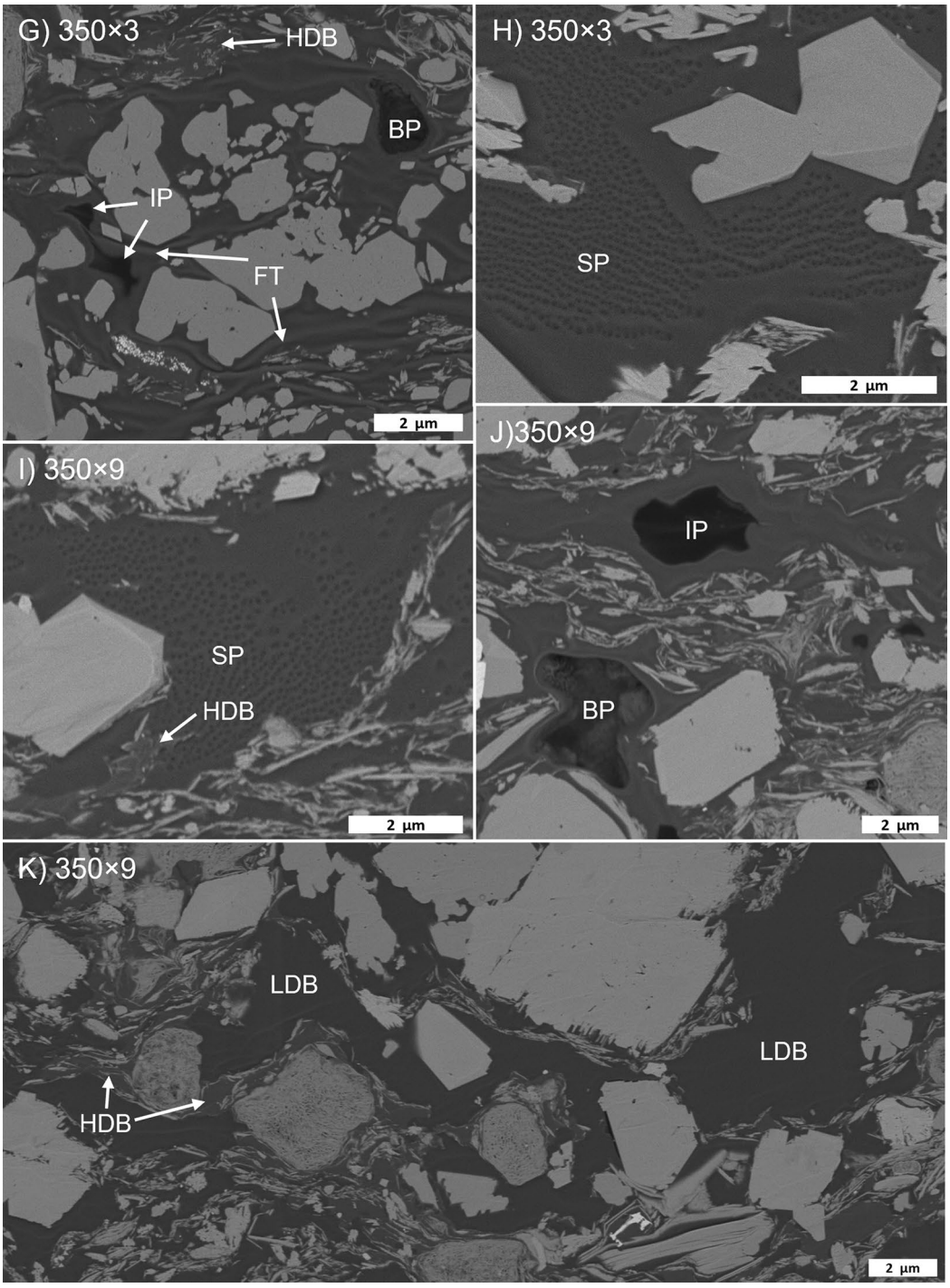

Figure 9. (continued)

VRo_{eqv}) relative to Type II samples (1.35% VRo_{eqv}). However, negative pore volume changes are minor and may just represent natural sample variation. The combined SEM and pore volume data suggest that porosity destruction by pore-filling solid bitumen may occur earlier in shales with Type IIS OM relative to those with Type II OM, but more investigation is warranted for a confident conclusion.

Pore size distribution (PSD). The PSD in artificially matured samples without overburden load, such as in the present study, should not be considered representative of *in-situ* rock properties. Compaction radically reduces pore volume at burial depths of 10 s to 100 s of meters in natural settings because water initially comprises up to 90% of the bulk volume of freshly deposited muds[3]. Furthermore, compaction-induced pore volume destruction is not limited to shallow burial or inorganic pore systems; organic porosity, at thousands of meters burial depth is also subject to compaction by overburden load or tectonic stress[28,29], particularly when volumes

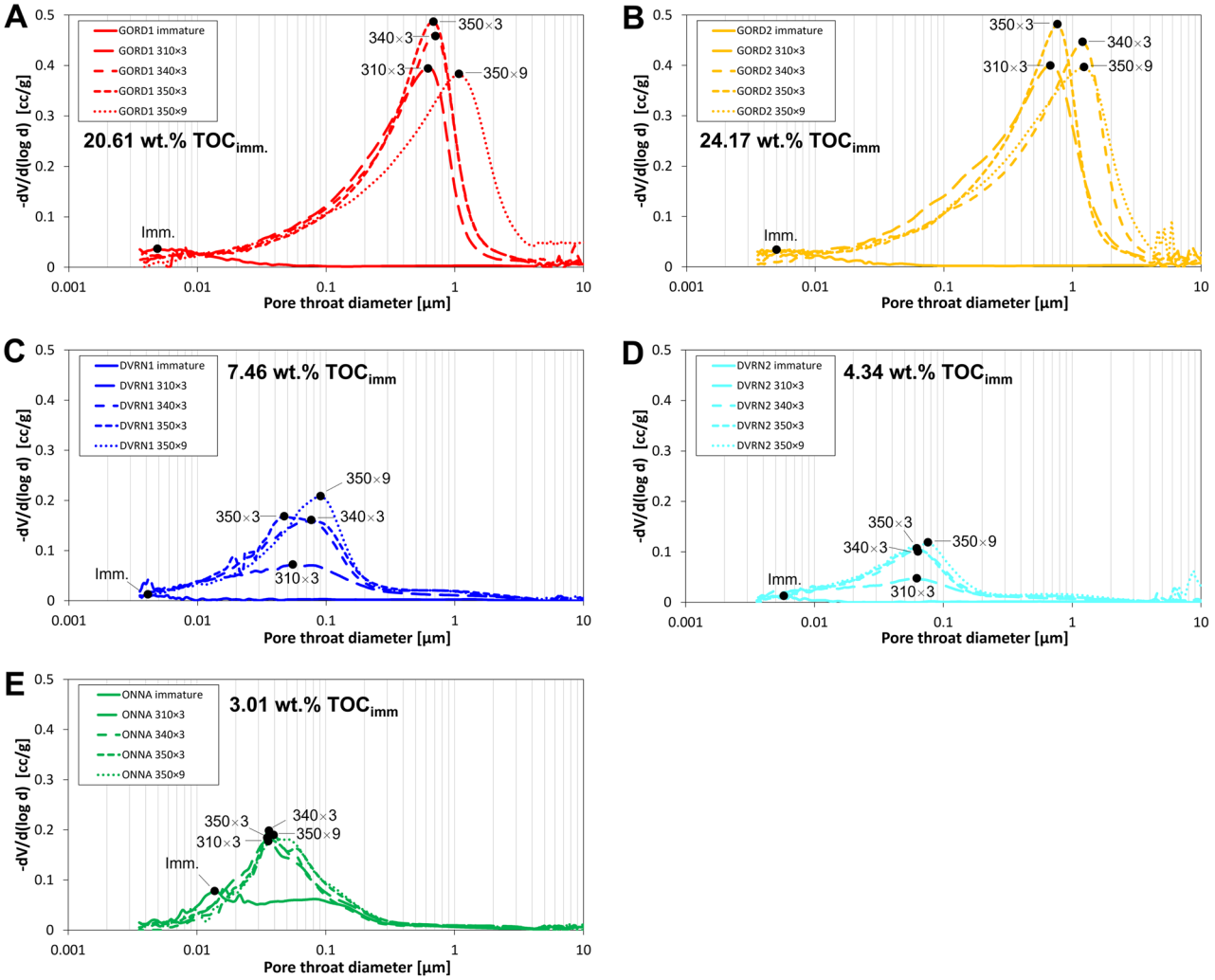

Figure 10. MICP pore throat size distributions for (**A**) GORD1, (**B**) GORD2, (**C**) DVRN1, (**D**) DVRN2 and (**E**) ONNA. Black circles indicate the peak pore throat diameter of each measurement. TOC_{imm}: measured TOC of immature samples.

of rigid matrix minerals are low. These processes, in addition to pore-filling by bitumen, are responsible for the extreme low pore volumes of immature samples reported here but had no influence on pores generated during hydrous pyrolysis.

That caveat aside, there is still considerable insight to be gained from PSD and pore types observed in artificially matured samples, particularly the relationships between pore body size, pore throat size, and rock fabric. Across samples, it is commonly observed that the large organic pores (i.e., bubble- and irregular-shaped) have sizes limited by adjacent minerals. Rock fabric—specifically the distances between minerals or inert OM—controls maximum organic pore body size and defines the size of pore throats through which penetrating fluids (including Hg) must pass to access organic pores. Large organic pores observed in SEM are typically several hundred nanometers to a few micrometers across in all samples, but MICP PTSD are highly variable between sample sets, and skewed to lower diameters in samples with restrictive matrix fabrics and discontinuous OM particles (i.e., DVRN and ONNA). Naturally-matured organic-rich mudstones likely also experience the phenomenon of rock fabric limiting access to organic pores unless OM is highly voluminous and continuous.

Conclusions

This study examined the influence of total organic sulfur (TOS) content on the generation of bitumen and secondary organic porosity in five sample groups of organic-rich mudstones from the Duvernay Formation (Canada), Onnagawa Formation (Japan), and Gordondale member of the Fernie Formation (Canada). Pore volume increase with thermal maturity was seen in all five sample groups, with the magnitude of pore volume generation increasing with increasing TOC. SEM observations confirmed that most pores generated during HP were organic pores. However, inorganic porosity, linked to the progressive alteration of dolomite to fibrous masses, a relatively novel observation, was illustrated as evidence that correlations between porosity and thermal maturity in organic-rich rocks cannot always be completely ascribed to organic porosity. The size ranges of organic pores were relatively

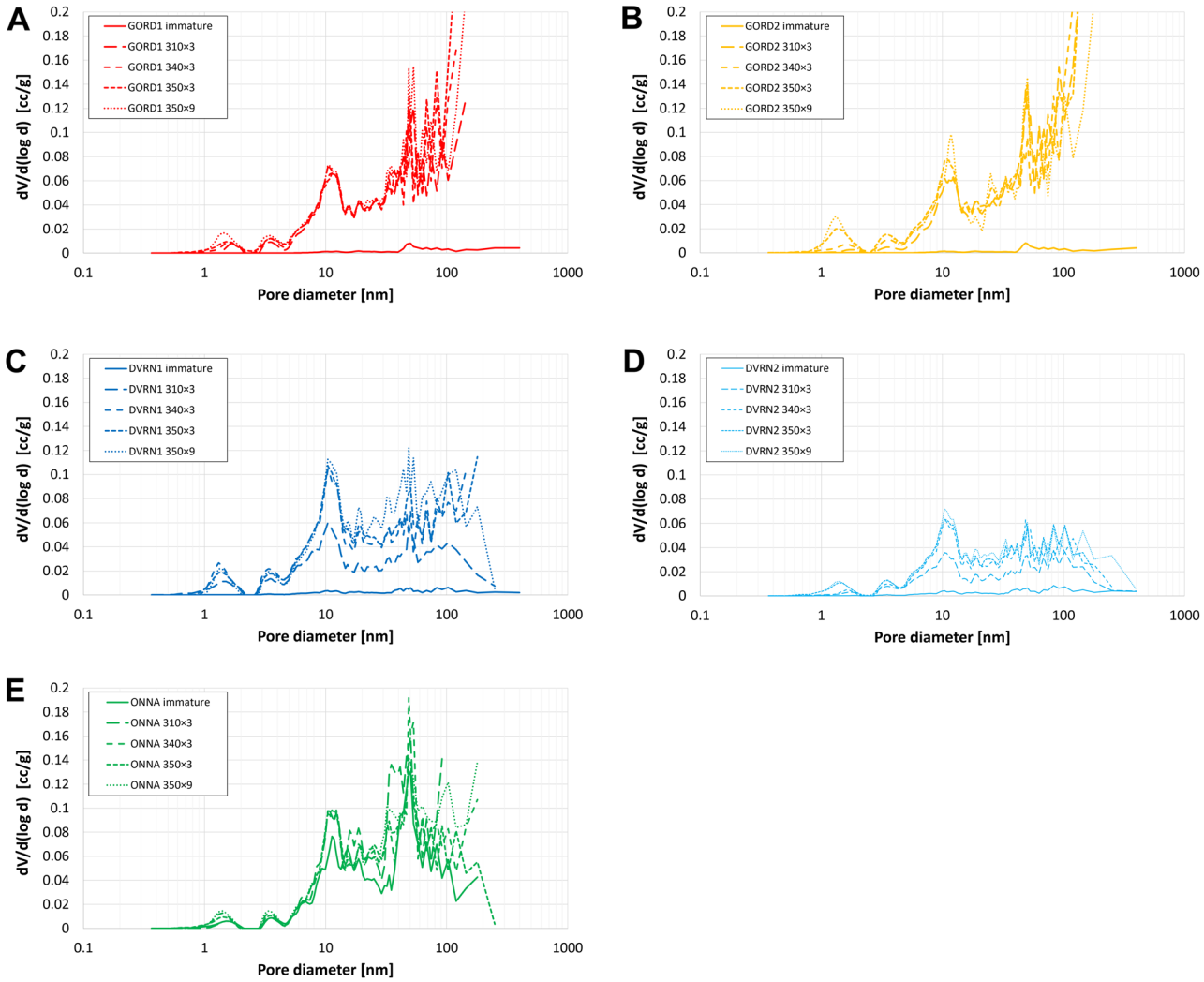

Figure 11. N_2-adsorption pore size distributions for (**A**) GORD1, (**B**) GORD2, (**C**) DVRN1, (**D**) DVRN2 and (**E**) ONNA.

constant across samples and thermal maturity, which was interpreted to be the result of the absence of compressive forces during thermal maturation. MICP PTSD was controlled by rock fabric, particularly the spacing between mineral grains, which constricted flow of Hg into organic pore networks.

Evaluations of the pore space using SEM, MICP, and N_2-adsorption support the hypothesis that organic porosity is created at lower thermal maturity in marine kerogen of Type IIS relative to Type II. This conclusion fits well with the rich history of literature that demonstrates early generation of liquid hydrocarbons in Type IIS source rocks and the present study is, to our knowledge, the first published demonstration of this phenomenon. This study is also novel in its illustration of solid bitumen occlusion of organic porosity, not only inorganic matrix porosity, which has not been well documented previously. Additionally, two distinct phases of solid bitumen generation were observed in SEM images and BRo measurements.

Methodology

Sample selection and workflow. Five thermally immature core samples were selected from three organic-rich mudstone units, which in order of increasing TOS content were the late Devonian Duvernay Formation (Canada), middle-late Miocene Onnagawa Formation (Japan), and early Jurassic Gordondale (formerly Nordegg) member of the Fernie Formation (Canada). Duvernay Formation mudstones are primarily calcareous to siliceous, as a function of high biogenic silica production and the deposition of reef- and shelf-derived fine-grained carbonate sediment deposited in an epicontinental seaway on the flooded passive margin of western North America[65–69]. The Onnagawa Formation is composed of siliceous, diatomaceous mudstones and siltstones that were deposited in deep, silled sub-basins in the paleo-Sea of Japan, under highly bioproductive surface waters driven by intense upwelling[70–72]. The Gordondale member is composed of organic-rich, phosphatic and highly radioactive calcareous-siliceous mudstones and fine-grained calcarenites[73,74]. that were deposited in an epicontinental seaway that occupied a subsiding foreland basin along the western Canadian Cordilleran margin[75].

Sample family	HP temperature and duration	Pore volume (cc/g)		Estimated porosity (%)	
		MICP	N_2	MICP	N_2
DVRN1	Immature	0.0063	0.0038	0.3	0.2
	310 °C × 3 days	0.0927	0.0487	3.9	2.0
	340 °C × 3 days	0.1553	0.0829	6.5	3.5
	350 °C × 3 days	0.1777	0.0860	7.4	3.6
	350 °C × 9 days	0.1686	0.0977	7.0	4.1
DVRN2	Immature	0.0045	0.0045	0.2	0.2
	310 °C × 3 days	0.0569	0.0303	2.4	1.3
	340 °C × 3 days	0.0919	0.0482	3.8	2.0
	350 °C × 3 days	0.0921	0.0545	3.8	2.3
	350 °C × 9 days	0.1092	0.0556	4.6	2.3
ONNA	Immature	0.0911	0.0594	3.8	2.5
	310 °C × 3 days	0.1463	0.0866	6.1	3.6
	340 °C × 3 days	0.1415	0.0887	5.9	3.7
	350 °C × 3 days	0.1536	0.0930	6.4	3.9
	350 °C × 9 days	0.1518	0.1016	6.3	4.2
GORD1	Immature	0.0141	0.0025	0.6	0.1
	310 °C × 3 days	0.3458	0.0696	14.4	2.9
	340 °C × 3 days	0.3599	0.0730	15.0	3.0
	350 °C × 3 days	0.3753	0.0793	15.6	3.3
	350 °C × 9 days	0.3965	0.0813	16.5	3.4
GORD2	Immature	0.0135	0.0022	0.6	0.1
	310 °C × 3 days	0.3942	0.0654	16.4	2.7
	340 °C × 3 days	0.4049	0.0736	16.9	3.1
	350 °C × 3 days	0.3821	0.0914	15.9	3.8
	350 °C × 9 days	0.4266	0.0822	17.8	3.4

Table 5. Measured pore volume and estimated porosity (assuming bulk density = 2.4 g/cc) from MICP and N_2-adsorption.

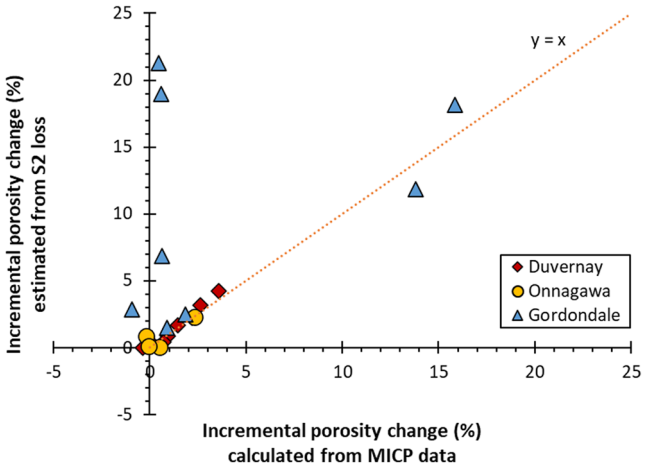

Figure 12. Comparison of incremental porosity change estimated from MICP and Rock–Eval S2.

Two Duvernay core samples were selected from the Long Run DD Gvillee 4–34–77–23 well at present-day burial depths of 2413.15 m and 2414.00 m. One Onnagawa core sample was selected at a depth of 16.57 m from a shallow science well in Akita Prefecture. Two Gordondale core samples were selected from the Adamant Berwyn 11–32–82–25 well at depths of 924.70 m and 926.00 m.

Each of the five core samples consisted of approximately 200 g of continuous core slab, representing 15–25 cm of vertical thickness (Fig. 14). Each sample was crushed to < 2.0 mm and homogenized then separated into 5 aliquots. Organic geochemical, mineralogical, petrophysical, and high-resolution imaging experiments were

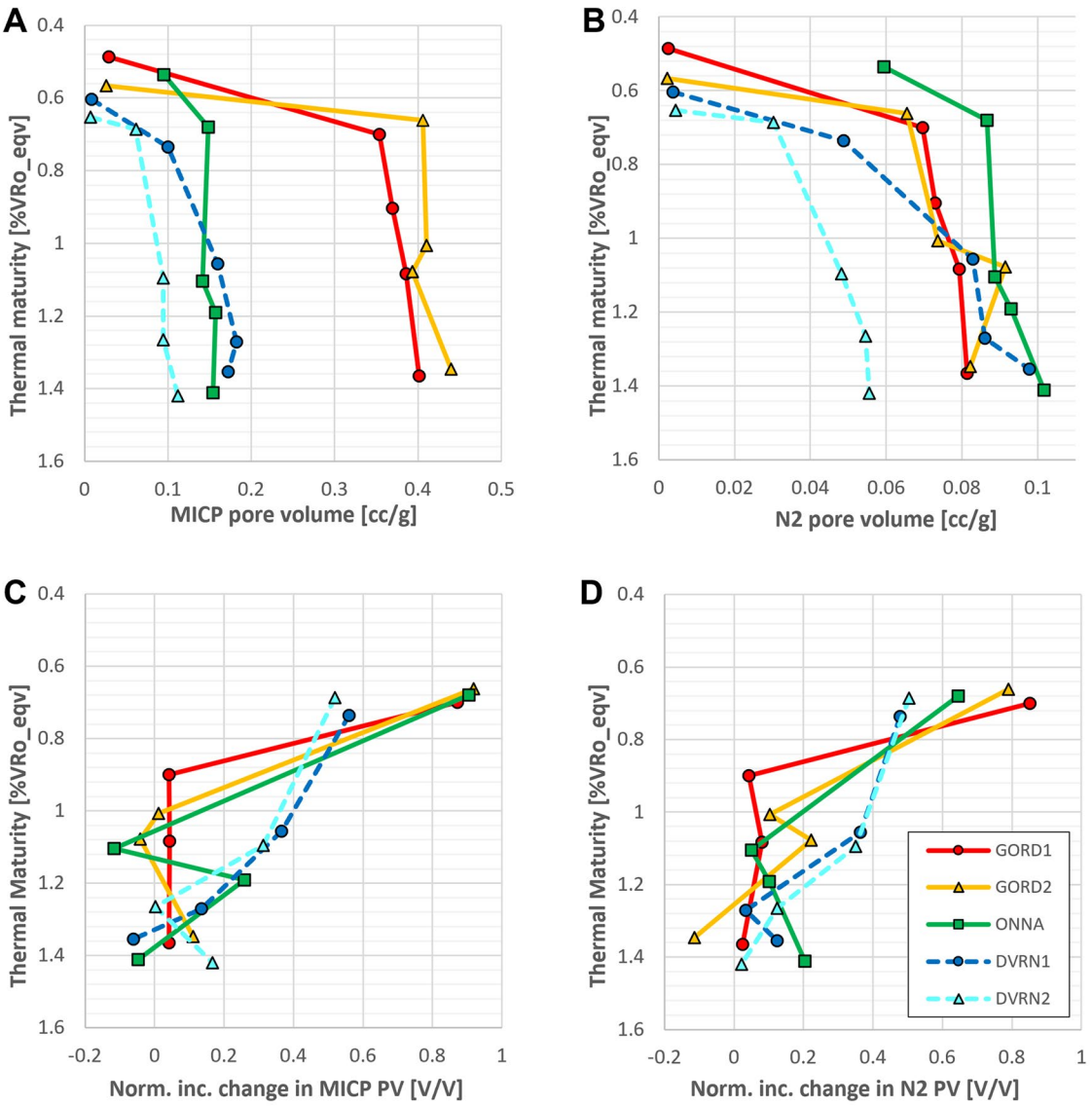

Figure 13. (**A**, **B**) Intruded pore volume from MICP (**A**) and N_2-adsorption (**B**) vs thermal maturity. Maturity increases down the y-axis as a proxy for burial depth. (**C**, **D**) Normalized incremental change in MICP (**C**) and N_2 (**D**) pore volume vs. thermal maturity. Normalized incremental PV change = $(PV_n - PV_{n-1})/(PV_{350\times9} - PV_{immature})$. Total porosity change from immature to maximum maturity was normalized to 1. Each data point represents the fraction of the total pore volume change that occurred at each maturity stage, and as such, there is no data for immature samples.

performed on thermally immature sample aliquots and on 4 additional aliquots of equivalent sample material at matured to successively higher thermal maturity stages through hydrous pyrolysis. A total of 25 unique samples were analyzed (5 core samples × 5 maturity stages) using the methods of organic petrology, HAWK programmed pyrolysis, X-ray diffraction (XRD), scanning electron microscopy (SEM), low pressure N_2 gas adsorption, and mercury injection capillary pressure (MICP). Sulfur analysis using Rock-Eval 7S was performed on only the immature sample aliquots. Elemental concentration maps of high-maturity samples were generated using energy-dispersive X-ray spectroscopy (SEM–EDS). Prior to mineralogical, textural, and petrophysical measurements, crushed sample material was cleaned using Dean Stark–Soxhlet extraction to remove soluble bitumen and lighter hydrocarbons.

Hydrous pyrolysis. Hydrous pyrolysis (HP) was performed to simulate *in-situ* thermal maturation using a 500 ml Parr reactor equipped with a pressure gauge. For each HP run, 40 g of homogenized crushed rock (2 mm particle size) and 100 ml distilled water were placed inside the reactor. The reactor was sealed and pressurized at 100 psi using inert argon gas. Separate HP runs were performed at isothermal temperatures of 310, 340, and 350 °C for 3 days and 350 °C for 9 days. Based on previous HP studies, the selected temperature range was within the simulated thermogenic hydrocarbon generation and early gas window[33,36,76–79]. After each run, the produced

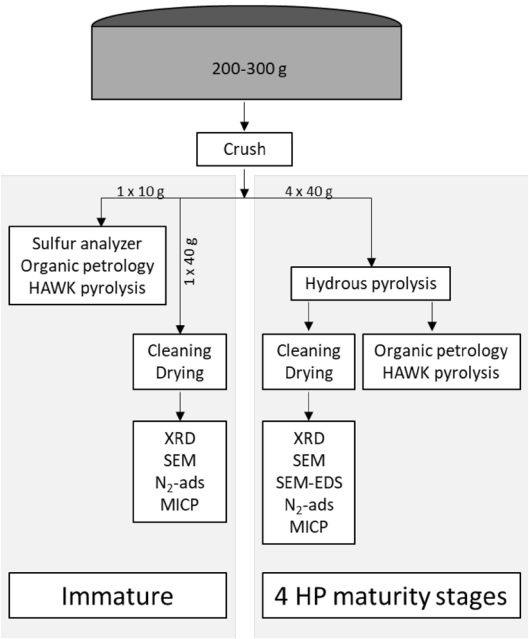

Figure 14. Workflow for sample processing and experimentation.

gas, oil, and rocks were collected separately and prepared for further analyses. The peak pressure ranged from 1475 psi = 100 atm @ 310 °C and 2675 psi = 182 atm @ 350 °C.

Total sulfur speciation. Approximately ~ 50 mg of bulk powder was analyzed using a Rock–Eval 7S analyzer (Vinci Technologies, France). The sulfur speciation analysis was performed using the basic/total sulfur method[80]. The temperature program was similar to the basic programmed pyrolysis method[81]. It started at a 300 °C iso-temperature for 3 min, followed by a 25 °C/min ramp to 652 °C, but with an extra oven step during the pyrolysis stage, which is a sulfur oven where the evolved gases are oxidized into SO_2 at 840 °C. Samples were then transferred to an oxidation oven with an extended analysis time during the oxidation stage and a 20 °C/min ramp from 300 to 1200 °C for decomposition of sulfate moieties[80,82]. The SO_2 gas released during both pyrolysis and oxidation stages was measured in real time by an ultraviolet (UV) detector. In addition to detection of total sulfur (TS) and total organic sulfur (TOS), the instrument separated and quantified pyritic sulfur (Fe-S), bitumen/oil organic sulfur (S1-S), organic sulfur associated with hydrocarbon prone kerogen (S2-S), and residual organic sulfur associated with oxidized OM (ROS or S4-S) and sulfate minerals. The basic programmed pyrolysis parameters such as S1, S2, S3, Tmax, and TOC were measured during the same process following the Behar et al. methodology[81].

Basic programmed pyrolysis. Bulk sediment samples (~ 70 mg) were analyzed by HAWK (Wildcat Technologies) programmed pyrolysis. The pyrolysis stage (under an N_2 environment) involved the initial iso-temperature of 300 °C for 3 min to release free hydrocarbons in the samples (S1, mg HC/g rock), followed by ramping the temperature up 25 °C/min to 650 °C to release, through thermal cracking, hydrocarbons and the oxygen contained in pyrolizable kerogen (S2, mg HC/g rock, and S3, mg CO_2/g rock, respectively). Samples were then automatically transferred to the oxidation oven and heated from 300 to 850 °C at a heating rate of 20 °C/min to measure the residual inert organic carbon (S4, mg CO, and CO_2/g rock and residual carbon (RC) wt%) and a portion of the mineral carbon (MinC, wt%).

Total organic carbon (TOC, wt%) was quantified as the sum of the total quantity of organic matter released during pyrolysis (pyrolizable carbon, PC wt%) and the oxidation step (residual carbon, RC wt.%). The oxygen index (OI) was calculated by normalizing the quantity of the pyrolizable CO_2 (S3) to total organic carbon (S3/TOC × 100) and is proportional to the elemental O/C ratio of the kerogen while the hydrogen index (HI) is the ratio of (S2/TOC × 100) and is proportional to H/C[81].

Organic petrology. Organic petrography was carried out on selected samples using polished blocks made with a cold-setting epoxy–resin mixture. The resulting sample pellets were ground and polished, in final preparation for microscopy, performed using an incident light Zeiss Axioimager II microscope system equipped with an ultraviolet (UV) light source and the Diskus-Fossil system. Fluorescence microscopy of organic matter was carried out using UV G 365 nm excitation with a 420 nm barrier filter. Random reflectance measurements were conducted under oil immersion (objective × 50) following ASTM methodology[83]. The standard reference for reflectance measurement was yttrium–aluminum-garnet with a standard reflectance of 0.906% under oil immersion.

Scanning electron microscopy and energy dispersive X-ray spectroscopy. Prior to mineralogical, textural, and petrophysical measurements, sample material was cleaned using Dean Stark–Soxhlet extraction. Toluene was percolated through the samples for three days and the produced water volumes were recorded in a graduated sidearm collection tube. Subsequently, samples were placed in effluent methyl alcohol (methanol) for one day and then in a methanol/chloroform (83% / 17%) azeotrope for 3 days. The samples were dried in a vacuum oven at 80 °C until daily weight measurements stabilized.

For scanning electron microscopy (SEM) approximately 0.5 g of crushed rock material was placed into shallow boreholes within cured epoxy pellets then epoxied in place. Pellets were slowly exposed to vacuum conditions for 20–30 s to conform the epoxy to the rock particle boundaries and prevent particles being dislodged during polishing. The epoxy in the pellets was allowed to cure over 24 h without heating. Pellets were trimmed to approximately $1 \times 1 \times 1$ cm then ground and pre-polished using a rotating abrasive wheel with fine silicon carbide sandpaper. Samples were then placed into a Fischione 1060 SEM Mill and the polished surface was ion milled using a broad argon ion beam (BIB) at low angle (relative to the sample surface). A very light carbon coating was sputtered onto the polished sample surface to reduce charging during SEM imaging. Imaging of polished surfaces was performed using a Helios NanoLab™ 650 Dual Beam™ microscope with an accelerating voltage of 2 kV and a probe current of 100 pA. All images are backscattered electron images. Twenty to 25 rock particles per pellet were imaged at 115 nm/px ("Overview") to screen for desirable bedding orientation, texture, surface quality, and organic richness. High-resolution (5 nm/px) imaging was performed on a 114×114 μm area of one particle in each pellet."Overview" and "high-res" images are mosaics of multiple stitched image tiles; stitching expands the field of view while maintaining spatial resolution.

Greyscale variation in the backscattered electron SEM images relates to average atomic mass, but it is also proportional to density of the OM because low density OM has a low C:H atomic ratio, i.e. more low-mass H atoms.

On the SEM pellets of the 350×9 samples, at the same locations as the high-resolution images, elemental concentration maps with a spatial resolution of 5 nm/px were generated using scanning electron microscopy with energy-dispersive X-ray spectroscopy (SEM–EDS). The instrument was a Helios NanoLab™ 650 Dual Beam™ SEM microscope with an EDS device. Data was collected with an accelerating voltage of 15 kV and a probe current of 0.8 nA.

Mercury injection capillary pressure and N_2-adsorption. Mercury injection capillary pressure (MICP) analysis was performed on 1 to 2 g of crushed rock using a Quantachrome Instruments PoreMaster 60GT. The measurement consisted of low-pressure analysis up to 50 psi and high-pressure analysis up to 60,000 psi for pore throat size distribution and pore volume estimation to a lower pore throat diameter limit of 3.6 nm.

Low pressure N_2 gas adsorption analysis was performed on approximately 1 g of crushed rock using a Micrtrac MRB BELSORP MAX II instrument. Before analysis, samples were heated at 100 °C for at least 4 h under diminished pressure. Measurement temperatures were kept to 77 K. Specific surface area and pore volume were evaluated using BET analysis. Pore size distribution was simulated by grand canonical Monte Carlo (GCMC).

Data availability

In addition to data tables and figures presented in the manuscript, variations of programmed pyrolysis parameters over the HP series of all samples are shown in Fig. S1 online. Fig. S2 contains SEM–EDS images confirming the Mg-rich composition of fibrous masses.

Received: 9 October 2022; Accepted: 15 May 2023
Published online: 19 June 2023

References

1. Jarvie, D. M. Shale resource systems for oil and gas: Part 1—shale-gas resource systems. In *Shale Reservoirs—Giant Resources for the 21st Century* Vol. 97 (ed. Breyer, J. A.) 69–87 (American Association of Petroleum Geologists, 2012).
2. Milliken, K. L., Rudnicki, M., Awwiller, D. N. & Zhang, T. Organic matter-hosted pore system, Marcellus formation (Devonian), Pennsylvania. *Am. Assoc. Pet. Geol. Bull.* **97**, 177–200 (2013).
3. Velde, B. Compaction trends of clay-rich deep sea sediments. *Mar. Geol.* **133**, 193–201 (1996).
4. Mondol, N. H., Bjørlykke, K., Jahren, J. & Høeg, K. Experimental mechanical compaction of clay mineral aggregates: Changes in physical properties of mudstones during burial. *Mar. Pet. Geol.* **24**, 289–311 (2007).
5. Aplin, A. C. & Macquaker, J. H. S. Mudstone diversity: Origin and implications for source, seal, and reservoir properties in petroleum systems. *Am. Assoc. Pet. Geol. Bull.* **95**, 2031–2059 (2011).
6. Lash, G. G. & Blood, D. Geochemical and textural evidence for early (shallow) diagenetic growth of stratigraphically confined carbonate concretions, Upper Devonian Rhinestreet black shale, western New York. *Chem. Geol.* **206**, 407–424 (2004).
7. Milliken, K. L., Esch, W. L., Reed, R. M. & Zhang, T. Grain assemblages and strong diagenetic overprinting in siliceous mudrocks, Barnett Shale (Mississippian), Fort Worth Basin, Texas. *Am. Assoc. Pet. Geol. Bull.* **96**, 1553–1578 (2012).
8. Milliken, K. L. & Day-Stirrat, R. J. Cementation in mudrocks: Brief review with examples from cratonic basin mudrocks. In *Critical Assessment of Shale Resource Plays* Vol. 103 (eds Chatellier, J. & Jarvie, D.) 133–150 (AAPG Memoir, 2013).
9. Milliken, K. L. & Olson, T. Silica diagenesis, porosity evolution, and mechanical behavior in siliceousmudstones, Mowry Shale (Cretaceous), Rocky Mountains, USA. *J. Sediment. Res.* **87**, 366–387 (2017).
10. Mathia, E. J., Rexer, T. F. T., Thomas, K. M., Bowen, L. & Aplin, A. C. Influence of clay, calcareous microfossils, and organic matter on the nature and diagenetic evolution of pore systems in mudstones. *J. Geophys. Res. Solid Earth* **124**, 149–174 (2019).
11. Loucks, R. G., Reed, R. M., Ruppel, S. C. & Jarvie, D. M. Morphology, genesis, and distribution of nanometer-scale pores in siliceous mudstones of the Mississippian Barnett shale. *J. Sediment. Res.* **79**, 848–861 (2009).
12. Curtis, M. E., Cardott, B. J., Sondergeld, C. H. & Rai, C. S. Development of organic porosity in the Woodford Shale with increasing thermal maturity. *Int. J. Coal. Geol.* **103**, 26–31 (2012).
13. Mastalerz, M., Schimmelmann, A., Drobniak, A. & Chen, Y. Porosity of Devonian and Mississippian New Albany Shale across a maturation gradient: Insights from organic petrology', gas adsorption, and mercury intrusion. *Am. Assoc. Pet. Geol. Bull.* **97**, 1621–1643 (2013).

14. Pommer, M. & Milliken, K. Pore types and pore-size distributions across thermal maturity, Eagle Ford Formation, Southern Texas. *AAPG Bull.* **99**, 1713–1744 (2015).
15. Cardott, B. J., Landis, C. R. & Curtis, M. E. Post-oil solid bitumen network in the Woodford Shale, USA: A potential primary migration pathway. *Int. J. Coal. Geol.* **139**, 106–113 (2015).
16. Camp, W. K. Diagenetic evolution of organic matter cements: Implications for unconventional shale reservoir quality prediction. In *Mudstone Diagenesis: Research Perspectives for Shale Hydrocarbon Reservoirs Seals and Source Rocks* Vol. 120 (eds Camp, W. K. *et al.*) 209–224 (AAPG, 2019).
17. Bernard, S., Wirth, R., Schreiber, A., Schulz, H. M. & Horsfield, B. Formation of nanoporous pyrobitumen residues during maturation of the Barnett Shale (Fort Worth Basin). *Int. J. Coal Geol.* **103**, 3–11 (2012).
18. Dong, T. *et al.* A model for porosity evolution in shale reservoirs: An example from the Upper Devonian Duvernay Formation, Western Canada Sedimentary Basin. *Am. Assoc. Pet. Geol. Bull.* **103**, 1017–1044 (2019).
19. Loucks, R. G. & Reed, R. M. Scanning-electron-microscope petrographic evidence for distinguishing organic-matter pores associated with depositional organic matter versus migrated organic matter in mudrock. *GCAGS J.* **3**, 51–60 (2014).
20. Sanei, H., Wood, J. M., Ardakani, O. H., Clarkson, C. R. & Jiang, C. Characterization of organic matter fractions in an unconventional tight gas siltstone reservoir. *Int. J. Coal Geol.* **150–151**, 296–305 (2015).
21. Wood, J. M., Sanei, H., Curtis, M. E. & Clarkson, C. R. Solid bitumen as a determinant of reservoir quality in an unconventional tight gas siltstone play. *Int. J. Coal Geol.* **150–151**, 287–295 (2015).
22. Wood, J. M., Sanei, H., Haeri-Ardakani, O., Curtis, M. E. & Akai, T. Organic petrography and scanning electron microscopy imaging of a thermal maturity series from the Montney tight-gas and hydrocarbon liquids fairway. *Bull. Can. Pet. Geol.* **66**, 499–515 (2018).
23. Akihisa, K. *et al.* Integrating mud gas and cuttings analyses to understand local CGR variation in the Montney tight gas reservoir. *Int. J. Coal. Geol.* **197**, 42–52 (2018).
24. Modica, C. J. & Lapierre, S. G. Estimation of kerogen porosity in source rocks as a function of thermal transformation: Example from the Mowry Shale in the Powder River Basin of Wyoming. *Am. Assoc. Pet. Geol. Bull.* **96**, 87–108 (2012).
25. Guo, X. *et al.* Comparison of pore systems of clay-rich and silica-rich gas shales in the lower Silurian Longmaxi formation from the Jiaoshiba area in the eastern Sichuan Basin, China. *Mar. Pet. Geol.* **101**, 265–280 (2019).
26. Dong, T. *et al.* Quartz types and origins in the paleozoic Wufeng-Longmaxi Formations, Eastern Sichuan Basin, China: Implications for porosity preservation in shale reservoirs. *Mar. Pet. Geol.* **106**, 62–73 (2019).
27. Fishman, N. S. *et al.* The nature of porosity in organic-rich mudstones of the Upper Jurassic Kimmeridge Clay Formation, North Sea, offshore United Kingdom. *Int. J. Coal Geol.* **103**, 32–50 (2012).
28. Knapp, L. J. *et al.* The influence of rigid matrix minerals on organic porosity and pore size in shale reservoirs: Upper Devonian Duvernay Formation, Alberta, Canada. *Int. J. Coal Geol.* **227**, 103525 (2020).
29. Ma, Y. *et al.* Possible pore structure deformation effects on the shale gas enrichment: An example from the Lower Cambrian shales of the Eastern Upper Yangtze Platform, South China. *Int. J. Coal Geol.* **217**, 103349 (2020).
30. Ma, Y. *et al.* Pore structure of the graptolite-derived OM in the Longmaxi Shale, southeastern Upper Yangtze Region, China. *Mar. Pet. Geol.* **72**, 1–11 (2016).
31. Ardakani, O. H. *et al.* Do all fractions of organic matter contribute equally in shale porosity? A case study from Upper Ordovician Utica Shale, southern Quebec, Canada. *Mar. Pet. Geol.* **92**, 794–808 (2018).
32. Liu, B., Schieber, J. & Mastalerz, M. Combined SEM and reflected light petrography of organic matter in the New Albany Shale (Devonian-Mississippian) in the Illinois Basin: A perspective on organic pore development with thermal maturation. *Int. J. Coal Geol.* **184**, 57–72 (2017).
33. Lewan, M. D. Evaluation of petroleum generation by hydrous phrolysis experimentation. *Philos. Trans. R. Soc. Lond. A* **315**, 123–134 (1985).
34. Orr, W. L. Kerogen/asphaltene/sulfur relationships in sulfur-rich Monterey oils. *Org. Geochem.* **10**, 499–516 (1986).
35. Baskin, D. K. & Peters, K. E. Early generation characteristics of a sulfur-rich monterey kerogen. *Am. Assoc. Pet. Geol. Bull.* **76**, 1306 (1992).
36. Lewan, M. D. & Ruble, T. E. Comparison of petroleum generation kinetics by isothermal hydrous and nonisothermal open-system pyrolysis. *Org. Geochem.* **33**, 1457–1475 (2002).
37. Lewan, M. D., Kotarba, M. J., Curtis, J. B., Wiecław, D. & Kosakowski, P. Oil-generation kinetics for organic facies with Type-II and -IIS kerogen in the Menilite Shales of the Polish Carpathians. *Geochim. Cosmochim. Acta* **70**, 3351–3368 (2006).
38. Schimmelmann, A., Lewan, M. D. & Wintsch, R. P. D/H isotope ratios of kerogen, bitumen, oil, and water in hydrous pyrolysis of source rocks containing kerogen types I, II, IIS, and III. *Geochim. Cosmochim. Acta* **63**, 3751–3766 (1999).
39. French, K. L., Birdwell, J. E. & Lewan, M. D. Trends in thermal maturity indicators for the organic sulfur-rich Eagle Ford Shale. *Mar. Pet. Geol.* **118**, 104459 (2020).
40. Liu, K. & Ostadhassan, M. The impact of pore size distribution data presentation format on pore structure interpretation of shales. *Adv. Geo-Energy Res.* **3**, 187–197 (2019).
41. Lafargue, E., Marquis, F. & Pillot, D. Rock-eval 6 applications in hydrocarbon exploration, production, and soil contamination studies. *Rev. l'Inst. Franc. Pet.* **53**, 421–437 (1998).
42. Jacob, H. Classification, structure, genesis and practical importance of natural solid oil bitumen ("migrabitumen"). *Int. J. Coal Geol.* **11**, 65–79 (1989).
43. van de Wetering, N., Sanei, H. & Mayer, B. Organic matter characterization in mixed hydrocarbon producing areas within the Duvernay Formation, Western Canada Sedimentary Basin, Alberta. *Int. J. Coal. Geol.* **156**, 1–11 (2016).
44. Waliczek, M., Machowski, G., Poprawa, P., Świerczewska, A. & Więcław, D. A novel VRo, Tmax, and S indices conversion formulae on data from the fold-and-thrust belt of the Western Outer Carpathians (Poland). *Int. J. Coal Geol.* **234**, 103672 (2021).
45. Jiang, C. *et al.* Hydrocarbon evaporative loss from shale core samples as revealed by Rock-Eval and thermal desorption-gas chromatography analysis: Its geochemical and geological implications. *Mar. Pet. Geol.* **70**, 294–303 (2016).
46. Peters, K. E. Guidelines for evaluating petroleum source rock using programmed pyrolysis'. *Am. Assoc. Pet. Geol. Bull.* **70**, 318–329 (1986).
47. Yang, S. & Horsfield, B. Critical review of the uncertainty of Tmax in revealing the thermal maturity of organic matter in sedimentary rocks. *Int. J. Coal Geol.* **225**, 103500 (2020).
48. Löhr, S. C., Baruch, E. T., Hall, P. A. & Kennedy, M. J. Is organic pore development in gas shales influenced by the primary porosity and structure of thermally immature organic matter?. *Org. Geochem.* **87**, 119–132 (2015).
49. Dong, H. M. *et al.* Impacts of organic structures and inherent minerals of coal on soot formation during pyrolysis. *Energies* **12**, 4410 (2019).
50. Baruch, E. T., Kennedy, M. J., Löhr, S. C. & Dewhurst, D. N. Feldspar dissolution-enhanced porosity in Paleoproterozoic shale reservoir facies from the Barney Creek Formation (McArthur Basin, Australia). *Am. Assoc. Pet. Geol. Bull.* **99**, 1745–1770 (2015).
51. Ardakani, O. H. *et al.* Hydrocarbon potential and reservoir characteristics of Lower Cretaceous Garbutt Formation, Liard Basin, Canada. *Fuel* **209**, 274–289 (2017).
52. Nie, H., Sun, C., Liu, G., Du, W. & He, Z. Dissolution pore types of the Wufeng Formation and the Longmaxi Formation in the Sichuan Basin, south China: Implications for shale gas enrichment. *Mar. Pet. Geol.* **101**, 243–251 (2019).

53. Wood, J. M. *et al.* Solid bitumen in the Montney Formation: Diagnostic petrographic characteristics and significance for hydrocarbon migration. *Int. J. Coal Geol.* **198**, 48–62 (2018).
54. Curiale, J. A. Origin of solid bitumens, with emphasis on biological marker results. *Org. Geochem.* **10**, 559–580 (1986).
55. Mastalerz, M., Drobniak, A. & Stankiewicz, A. B. Origin, properties, and implications of solid bitumen in source-rock reservoirs: A review. *Int. J. Coal Geol.* **195**, 14–36 (2018).
56. Sanei, H. Genesis of solid bitumen. *Sci. Rep.* **10**, 1–10 (2020).
57. Valentine, B. J., Hackley, P. C. & Hatcherian, J. J. Hydrous pyrolysis of New Albany Shale: A study examining maturation changes and porosity development. *Mar. Pet. Geol.* **134**, 105368 (2021).
58. Liu, K. *et al.* Experimental study on the impact of thermal maturity on shale microstructures using hydrous pyrolysis. *Energy Fuels* **33**, 9702–9719 (2019).
59. Wang, Y. *et al.* Nanoscale pore network evolution of xiamaling marine shale during organic matter maturation by hydrous pyrolysis. *Energy Fuels* **34**, 1548–1563 (2020).
60. Chen, J. & Xiao, X. Evolution of nanoporosity in organic-rich shales during thermal maturation. *Fuel* **129**, 173–181 (2014).
61. Guo, H., Jia, W., Peng, P., Zeng, J. & He, R. Evolution of organic matter and nanometer-scale pores in an artificially matured shale undergoing two distinct types of pyrolysis: A study of the Yanchang Shale with Type II kerogen. *Org. Geochem.* **105**, 56–66 (2017).
62. Suwannasri, K., Vanorio, T. & Clark, A. Monitoring the changes in the microstructure and the elastic and transport properties of Eagle Ford marl during maturation. *Geophysics* **83**, 263–281 (2018).
63. Wang, G. Deformation of organic matter and its effect on pores in mud rocks. *Am. Assoc. Pet. Geol. Bull.* **103**, 21–36 (2020).
64. Cao, T. *et al.* Pore formation and evolution of organic-rich shale during the entire hydrocarbon generation process: Examination of artificially and naturally matured samples. *J. Nat. Gas Sci. Eng.* **93**, 104020 (2021).
65. Switzer, S. B. *et al.* Devonian Woodbend-Winterburn strata of the Western Canada Sedimentary Basin. in *Geological Atlas of the Western Canada Sedimentary Basin* (eds. Mossop, G. D. & Shetsen, I.) 165–202 (Geological Survey of Canada, 1994).
66. Knapp, L. J., McMillan, J. M. & Harris, N. B. A depositional model for organic-rich Duvernay Formation mudstones. *Sediment. Geol.* **347**, 160–182 (2017).
67. Knapp, L. J., Harris, N. B. & McMillan, J. M. A sequence stratigraphic model for the organic-rich Upper Devonian Duvernay Formation, Alberta, Canada. *Sediment. Geol.* **387**, 152–181 (2019).
68. Harris, N. B., McMillan, J. M., Knapp, L. J. & Mastalerz, M. Organic matter accumulation in the Upper Devonian Duvernay Formation, Western Canada Sedimentary Basin, from sequence stratigraphic analysis and geochemical proxies. *Sediment. Geol.* **376**, 185–203 (2018).
69. Dong, T., Harris, N. B., Knapp, L. J., McMillan, J. M. & Bish, D. L. The effect of thermal maturity on geomechanical properties in shale reservoirs: An example from the Upper Devonian Duvernay Formation, Western Canada Sedimentary Basin. *Mar. Pet. Geol.* **97**, 137–153 (2018).
70. Koizumi, I., Sato, M. & Matoba, Y. Age and significance of Miocene diatoms and diatomaceous sediments from northeast Japan. *Palaeogeogr. Palaeoclimatol. Palaeoecol.* **272**, 85–98 (2009).
71. Martizzi, P., Chiyonobu, S., Hibi, Y., Yamato, H. & Arato, H. Middle–late Miocene paleoenvironment of the Japan sea inferred by sedimentological and geochemical characterization of coeval sedimentary rocks. *Mar. Pet. Geol.* **128**, 105059 (2021).
72. Tada, R. Origin of rhythmical bedding in middle Miocene siliceous rocks of the Onnagawa Formation, northern Japan. *J. Sediment. Res.* **61**, 1123–1145 (1991).
73. Asgar-Deen, M., Hall, R. & Riediger, C. The Gordondale Member: Designation of a new member in the Fernie Formation to replace the informal 'Nordegg Member' nomenclature of the subsurface of west-central Alberta. *Bull. Can. Pet. Geol.* **52**, 201–214 (2004).
74. Ross, D. J. K. & Bustin, R. M. Sediment geochemistry of the Lower Jurassic Gordondale Member, northeastern British Columbia. *Bull. Can. Pet. Geol.* **54**, 337–365 (2006).
75. Ettensohn, F. R. Assembly and dispersal of Pangea: Large-scale tectonic effects on coeval deposition of North American, marine, epicontinental, black shales. *J. Geodyn.* **23**, 287–309 (1997).
76. Lewan, M. D. Laboratory Simulation of Petroleum Formation. in *Organic Geochemistry* (eds. Engel, M. H. & Macko, S. A.) vol. 11, 419–442 (Springer, 1993).
77. Jiang, C. *et al.* Cyclopentanones and 2-cyclopenten-1-ones as major products of hydrous pyrolysis of immature organic-rich shales. *Org. Geochem.* **122**, 126–139 (2018).
78. Reyes, J. *et al.* Organic petrographic analysis of artificially matured chitinozoan- and graptolite-rich Upper Ordovician shale from Hudson Bay Basin, Canada. *Int. J. Coal Geol.* **199**, 138–151 (2018).
79. Spigolon, A. L. D., Lewan, M. D., de Barros Penteado, H. L., Coutinho, L. F. C. & Mendonça Filho, J. G. Evaluation of the petroleum composition and quality with increasing thermal maturity as simulated by hydrous pyrolysis: A case study using a Brazilian source rock with Type I kerogen. *Org. Geochem.* **83–84**, 27–53 (2015).
80. Aboussou, A. *et al.* Pyritic sulphur and organic sulphur quantification in organic rich sediments using rock-eval. In *1st EAGE/IFPEN Conference on Sulfur Risk Management in Exploration and Production, SRM 2018* (European Association of Geoscientists and Engineers, EAGE, 2018).
81. Behar, F., Beaumont, V., De, H. L. & Penteado, B. Rock-Eval 6 technology: Performances and developments. *Oil Gas Sci. Technol. Rev.* **56**, 111–134 (2001).
82. Carvajal-Ortiz, H., Gentzis, T. & Ostadhassan, M. Sulfur differentiation in organic-rich shales and carbonates via open-system programmed pyrolysis and oxidation: Insights into fluid souring and H2S production in the Bakken shale, United states. *Energy Fuels* **1**, 01562 (2021).
83. ASTM. *Standard Test Method for Microscopical Determination of the Reflectance of Vitrinite Dispersed in Sedimentary Rocks D7708-14. ASTM* (2014).

Acknowledgements

This project was a joint study funded by Natural Resources Canada (NRCan) and Japan Organization for Metals and Energy Security (JOGMEC). The NRCan Geoscience for New Energy Supply (GNES) program partially funded this study (331403). The NRCan contribution number is 20220269. We would like to thank P. Webster and R. Vandenberg of the Geological Survey of Canada and the many laboratory staff at JOGMEC's Technology Research Center for their efforts in sample preparation and analysis.

Author contributions

L.J.K. and O.H.A. conceptualized the study and led the investigation. Data collection was carried out by O.H.A., J.R., and several laboratory personnel. Data interpretation, figure drafting, and manuscript preparation was led by L.J.K. and O.H.A. with significant contributions from J.R. and K.I.

Competing interests

The authors declare no competing interests.

Additional information

Supplementary Information The online version contains supplementary material available at https://doi.org/10.1038/s41598-023-35259-5.

Correspondence and requests for materials should be addressed to L.J.K.

Reprints and permissions information is available at www.nature.com/reprints.

Publisher's note Springer Nature remains neutral with regard to jurisdictional claims in published maps and institutional affiliations.